

Pure and Applied Geophysics

Seismic Tomography of the Southern California plate boundary region from noise-based Rayleigh and Love Waves

--Manuscript Draft--

Manuscript Number:	
Full Title:	Seismic Tomography of the Southern California plate boundary region from noise-based Rayleigh and Love Waves
Article Type:	Report-Top.Vol. Crustal Fault Zones
Keywords:	Noise-based imaging, Rayleigh and Love waves, San Jacinto fault zone region, velocity contrasts, low velocity zones, azimuthal anisotropy
Corresponding Author:	Dimitri Zigone, Ph.D. University of Southern California Los Angeles, California UNITED STATES
Corresponding Author Secondary Information:	
Corresponding Author's Institution:	University of Southern California
Corresponding Author's Secondary Institution:	
First Author:	Dimitri Zigone, Ph.D.
First Author Secondary Information:	
Order of Authors:	Dimitri Zigone, Ph.D. Yehuda Ben-Zion Michel Campillo Philippe Roux
Order of Authors Secondary Information:	
Abstract:	<p>We use cross correlations of ambient seismic noise between pairs of 158 broadband and short period sensors to investigate the velocity structure over the top 7 km of the crust in the Southern California plate boundary region around the San Jacinto Fault Zone (SJFZ). We derive from the 9-component correlation tensors associated with all station pairs dispersion curves of Rayleigh and Love wave group velocities. The dispersion results are inverted first for Rayleigh and Love waves group velocities maps and then for shear wave velocities on a 1.5 km² grid that includes portions of the SJFZ, the San Andreas Fault (SAF) and the Elsinore fault. The distributions of the Rayleigh and Love group velocities exhibit 2θ azimuthal anisotropy with fast directions parallel to the main faults and rotations in complex areas. The reconstructed 3D shear velocity model reveals complex shallow structures that are correlated with the main geological units, and show strong velocity contrasts across various fault sections along with low velocity damage zones and basins. The SJFZ is marked by a clear velocity contrast with higher Vs values on the NE block for the section SE of the San Jacinto basin and a reversed contrast across the section between the San Jacinto basin and the SAF. Velocity contrasts are also observed along the southern parts on the SAF and Elsinore fault, with a faster southwest block in both cases. The region around the Salton Trough is associated with a significant low velocity zone. Strong velocity reductions following flower-shape with depth are observed extensively around both the SJFZ and the SAF, and are especially prominent in areas of geometrical complexity. In particular, the area between the SJFZ and the SAF is associated with extensive low velocity zone that is correlated with diffuse seismicity at depth, and similar pattern including correlation with deep diffuse seismicity is observed at a smaller scale in the trifurcation area of the SJFZ. The results augment local earthquake tomography images that have low resolution in the top few km of the crust, and provide important constraints for studies concerned with behavior of earthquake ruptures, generation of rock damage and seismic shaking hazard in the region.</p>

Suggested Reviewers:	Fan-Chi Lin gilllin2@gmail.com
	German Prieto gprieto@mit.edu
	Haijiang Zhang hzhang.ustc@gmail.com
	Toshiro Tanimoto toshiro@geol.ucsb.edu

1 **Seismic Tomography of the Southern California plate boundary region from noise-**
2 **based Rayleigh and Love Waves**

3
4 3
5
6
7 4 Dimitri Zigone¹, Yehuda Ben-Zion¹, Michel Campillo² and Philippe Roux²
8
9

10 5
11
12 6 ¹Department of Earth Sciences, University of Southern California, Los Angeles, CA 90089-
13 7 0740, USA
14
15

16
17 8 ²Institut des Sciences de la Terre, Université Joseph Fourier, CNRS, IRD, BP 53, 38041
18

19
20 9 Corresponding author: zigone@usc.edu
21

22 10
23
24
25 11
26
27 12
28
29
30 13
31
32 14
33
34 15
35
36 16
37 16 *Pure Appl. Geophys.*
38
39 17 **in review 2014**
40
41 18
42
43 19
44
45 20
46
47 21 **Keywords:** Noise-based imaging, Rayleigh and Love waves, San Jacinto fault zone region,
48
49 22 velocity contrasts, low velocity zones, azimuthal anisotropy
50
51 23
52
53
54
55
56
57
58
59
60
61
62
63
64
65

24 **ABSTRACT**

1
2
3 25 We use cross correlations of ambient seismic noise between pairs of 158 broadband and
4 26 short period sensors to investigate the velocity structure over the top 7 km of the crust in the
5
6 27 Southern California plate boundary region around the San Jacinto Fault Zone (SJFZ). We
7
8 28 derive from the 9-component correlation tensors associated with all station pairs dispersion
9
10 29 curves of Rayleigh and Love wave group velocities. The dispersion results are inverted first
11
12 30 for Rayleigh and Love waves group velocities maps and then for shear wave velocities on a
13
14 31 1.5 km² grid that includes portions of the SJFZ, the San Andreas Fault (SAF) and the Elsinore
15
16 32 fault. The distributions of the Rayleigh and Love group velocities exhibit 2θ azimuthal
17
18 33 anisotropy with fast directions parallel to the main faults and rotations in complex areas. The
19
20 34 reconstructed 3D shear velocity model reveals complex shallow structures that are correlated
21
22 35 with the main geological units, and show strong velocity contrasts across various fault
23
24 36 sections along with low velocity damage zones and basins. The SJFZ is marked by a clear
25
26 37 velocity contrast with higher Vs values on the NE block for the section SE of the San Jacinto
27
28 38 basin and a reversed contrast across the section between the San Jacinto basin and the SAF.
29
30 39 Velocity contrasts are also observed along the southern parts on the SAF and Elsinore fault,
31
32 40 with a faster southwest block in both cases. The region around the Salton Trough is associated
33
34 41 with a significant low velocity zone. Strong velocity reductions following flower-shape with
35
36 42 depth are observed extensively around both the SJFZ and the SAF, and are especially
37
38 43 prominent in areas of geometrical complexity. In particular, the area between the SJFZ and
39
40 44 the SAF is associated with extensive low velocity zone that is correlated with diffuse
41
42 45 seismicity at depth, and similar pattern including correlation with deep diffuse seismicity is
43
44 46 observed at a smaller scale in the trifurcation area of the SJFZ. The results augment local
45
46 47 earthquake tomography images that have low resolution in the top few km of the crust, and
47
48 48 provide important constraints for studies concerned with behavior of earthquake ruptures,
49
50 49 generation of rock damage and seismic shaking hazard in the region.
51

51 **1. INTRODUCTION**

52
53
54 52 Crustal fault zones have complex distributions of seismic properties that may include
55
56 53 hierarchical damage zones, bimaterial interfaces, deformation structures such as basins and
57
58 54 ridges, and adjacent blocks with various geological units and multi-scale heterogeneities.
59
60 55 Imaging of the fault zone velocity structure and the surrounding environment can provide
61
62
63
64
65

56 important information for numerous topics ranging from the long-term evolution of the fault
57 system to likely earthquake behavior and expected seismic shaking hazard (e.g. Ben-Zion
58 2008, and references therein). In this study we present noise-based tomography of the shallow
59 crust in the Southern California plate boundary region, with a focus on the San Jacinto Fault
60 Zone (SJFZ). The results complement recent double-difference tomography of earthquake
61 arrival times in the area that show clearly along-strike and depth variations of fault damage
62 zones, velocity contrasts and other features of interest over the depth range of about 3-15 km
63 (Allam and Ben-Zion, 2012; Allam et al. 2014). The noise-based tomography of the present
64 work allows us to obtain reliable results in the top few km, where the earthquake ray-coverage
65 is sparse, and also to image a somewhat broader region than that analyzed in the above
66 double-difference tomography studies. Imaging the top few km of the crust is particularly
67 important for understanding site effects that can influence significantly the near-fault seismic
68 ground motion (e.g. Boore 2014; Kurzon et al. 2014).

69 Ambient noise tomography has developed considerably in recent years (see, e.g.,
70 Campillo et al., 2011, and references therein). Instead of using transient sources, noise-based
71 imaging involves extracting phase information between pairs of stations from correlations of
72 a diffuse random wavefield. Shapiro and Campillo (2004) and later works showed that the
73 dispersions curves extracted from noise correlation functions are similar to those obtained
74 from earthquakes. This allows the use of conventional surface wave tomography techniques
75 to produce group or phase velocity maps of regions covered by dense seismic network (e.g.
76 Shapiro et al., 2005; Sabra et al., 2005a,b; Lin et al., 2007, 2008; Moschetti et al., 2007; Yang
77 et al., 2007; Stehly et al., 2009; Roux et al., 2011). The primary advantage of this method is
78 the existence of ambient seismic noise in all places, albeit with strong spatio-temporal
79 variations (e.g. Stehly et al. 2006; Kimman and Trampert 2010; Landès et al. 2010; Hillers
80 and Ben-Zion 2011) that should be accounted for in the imaging analysis.

81 A recent study by Hillers et al. (2013) explored the feasibility of using ambient noise
82 correlations to image the shallow structures of the SJFZ region. They found that the noise
83 field in that area is sufficiently sensitive to the existing structures and that consistent velocity
84 measurements can be extracted from the cross-correlations of the ambient seismic noise. In
85 the following sections we perform detailed analysis of noise cross correlations using 158
86 stations in the plate-boundary region in southern CA. The noise cross correlations are
87 processed to retrieve Rayleigh and Love waves Green's functions, which are then used to
88 obtain tomographic images of the region. In the next section we describe briefly the area

89 under investigation and results from previous imaging studies. In Section 3 we outline the
90 data and pre-processing used to compute the cross correlations, and discuss potential effects
91 of the directivity of noise sources on the cross-correlation functions. In Section 4 we describe
92 the methods used to extract dispersion curves from the cross correlations and azimuthal
93 anisotropy of the group velocity measurements. In section 5 we discuss and tomography
94 formalism applied for inverting the dispersion results to shear wave velocities, and present the
95 obtained tomographic images for the plate boundary region around the SJFZ. The results are
96 discussed and summarized in section 6.

98 2. THE STUDY AREA

99 The San Jacinto fault zone (Figure 1) is one of several major right-lateral strike-slip
100 structures over which the motion between the North American and Pacific plates is
101 accommodated in southern California. It formed 1-2 million years ago, presumably in
102 response to geometrical complexities on the San Andreas Fault (SAF) such as the San
103 Gorgonio bend (e.g., Morton and Matti, 1993; Fialko et al., 2005; Janecke et al., 2010), and is
104 currently the most seismically active fault zone in southern California (Hauksson, 2012). The
105 SJFZ effectively straightens the boundary between the North America and Pacific plates, and
106 at present carries a slip rate that is comparable to that of the southern SAF (e.g., Fay and
107 Humphreys, 2005; Lindsey and Fialko, 2013). A smaller part of the plate motion in the area is
108 also accommodated by the Elsinore Fault located southwest of the SJFZ.

109 The structurally complex SJFZ consists of multiple segments (Fig. 1), which have distinct
110 surface expressions, and exhibit different seismic and geometrical properties (e.g., Lewis et
111 al., 2005; Wechsler et al., 2009, Salisbury et al., 2012). Over the past 1.5 Ma the fault has
112 accommodated roughly 24km of total displacement (Sharp, 1967; Rockwell et al. 1990; Kirby
113 et al., 2007). The central portion of the SJFZ, often called the Anza section, is the most
114 geometrically simple region with only a single active surface trace, the Clark Fault (CL).
115 Paleoseismic trench sites at various locations along the Clark Fault indicate that it has a
116 complicated rupture history featuring both large through-going events as well as segmented
117 smaller ruptures (Salisbury et al., 2012; Marilyani et al., 2013; Rockwell et al. 2014). The
118 Anza section has a clear across-fault velocity contrast over the seismogenic zone (Allam and
119 Ben-Zion 2012) and asymmetry of rock damage in the shallow crust based on the
120 tomographic images as well as direct small-scale geological mapping (Dor et al. 2006).

121 Southeast of Anza is the Trifurcation Area, where the Coyote Creek (CC) and Buck Ridge
122 (BR) segments branch off at low angles from the Clark fault. Though they vary in age and
123 cumulative slip, all three segments are currently seismically active, as evidenced by a cloud of
124 distributed seismicity throughout the Trifurcation Area. The complicated geometry is likely
125 also responsible for the highly heterogeneous focal mechanisms (Bailey et al., 2010;
126 Hauksson et al., 2012) in that region. Pronounced lithology contrasts are observed at the
127 surface geology across all three fault strands (Sharp, 1967; Morton et al., 2012), with contacts
128 between sedimentary and crystalline rocks in a variety of along-strike locations. The double-
129 difference tomographic images show clear velocity contrasts across all three faults, and about
130 4 km-wide low velocity zone with high V_P/V_S ratio in the trifurcation itself (Allam and Ben-
131 Zion, 2012; Allam et al., 2014). Detailed studies examining the geomorphology (Wechsler et
132 al., 2009) and seismic trapping structures (Lewis et al., 2005; Yang and Zhu 2010) in the area
133 demonstrated the existence of asymmetric rock damage in the shallow crust, with more
134 damage on the NE sides of each fault.

135 Northwest of Anza is the Hemet Stepover, a releasing step associated with the San Jacinto
136 basin, where slip is transferred from the Claremont segment to the Casa Loma-Clark segment.
137 Though the surface traces are distinct, paleoseismic work indicates that the two segments can
138 rupture in a single through-going event (e.g., Salisbury et al., 2012; Rockwell et al., 2006;
139 Marilyani et al., 2013). Compressional features at the Northwestern tip of the Casa Loma fault
140 (Ben-Zion et al., 2012), in an area of otherwise extensional deformation, demonstrate the
141 complexity of the system as a whole. The seismicity to the southeast of the Hemet Stepover is
142 diffuse and associated with several oblique-slip anastomosing fault segments partly
143 responsible for the uplift of the San Jacinto and Santa Rosa Mountains (Onderdonk, 1998).
144 This complex region is associated with about 10 km wide zone of low seismic velocities,
145 variations of the velocity contrast across the fault, and low V_P/V_S ratio around the San Jacinto
146 basin (Allam and Ben-Zion 2012; Allam et al. 2014).

147 The SJFZ joins the SAF at its northern termination at Cajon Pass where both faults cut
148 through the Transverse Ranges. The pass separates the San Bernardino Mountains to the east
149 from the San Gabriel range to the west. The presence of the San Bernardino basin leads to a
150 reversal of the velocity contrast across portions of the SJFZ in that section and various other
151 complexities (Allam and Ben-Zion 2012). Geologically mapped surface traces of the SJFZ
152 and the SAF at the junction are separated by a few km, but along-fault variations of slip
153 suggest that the fault systems are linked, with strain transfer onto the SJFZ probably

154 contributing to the decrease in slip on the SAF from 24+-3.5 mm/yr at Cajon Pass down to 5-
155 10 mm/yr at San Gorgonio Pass to the southeast (Dair and Cooke, 2009; Seeber and
156 Armbruster, 1995; Zoback and Healy, 1992). The junction also marks a transition from a
157 vertical SAF to the North to a dip that has been inferred to be as shallow as 37+-5° to the
158 south (Fuis et al., 2012). Seismicity patterns in the region around Cajon Pass are complicated,
159 with abrupt across-fault steps in maximum hypocentral depth (Magistrale and Sanders, 1996;
160 Yule and Sieh, 2003).

3. DATA, NOISE PROCESSING AND CROSS CORRELATIONS

3.1 Data and Noise pre-processing

164 We use continuous seismic data recorded during 2012, from January 1 to December 31, at
165 158 stations (Figure 1) of the various seismic networks of southern California (the California
166 Integrated Seismic network, the Anza network, the UC Santa Barbara Engineering
167 Seismology Network and the SJFZ Continental Dynamics project network). The combined
168 network includes broadband (sampling rate 40 Hz) and short period (200 Hz) sensors
169 distributed over the plate boundary region in southern California with inter-stations distances
170 ranging from 20 meters up to 288 km.

171 Imaging the subsurface structure using noise-based surface wave tomography requires
172 pre-processing and multiple analysis steps to increase the quality of determining phase
173 arrivals and dispersion curves (e.g. Shapiro & Campillo 2004; Bensen et al., 2007; Poli et al.,
174 2012; Boué et al., 2013). In the following, we apply a modified version of the pre-processing
175 procedure of Poli et al. (2012), which uses energy tests on short time windows in order to
176 remove the effects of transient sources (earthquakes) and instrumental problems (gaps). We
177 found by experimenting with the method version described below that it provides an efficient
178 tool for producing time series without obvious earthquake signals, in our study area with high
179 seismic activity, leading to cross correlations with high signal-to-noise ratio (SNR, defined
180 here as maximum amplitude divided by the standard deviation of the noise).

181 The signal pre-processing is done station by station in the following order: (1) the 24-hr
182 records are deconvolved from the instrument responses to ground velocity; (2) the data are
183 high-pass filtered at 100s and are clipped at 15 standard deviation to remove glitches due to
184 the digitalization; (3) the 24-hr traces are then cut in 4 hr sub-segments on which selection

185 tests are performed in order to remove additional instrumental problems and transient sources
186 like earthquakes. If the number of gaps exceeds 10% of a sub-segment, the segment is
187 removed. All segments with energy (integral over the segment of the waveform amplitude
188 square) larger than twice the standard deviation of energy over the entire day are removed. (4)
189 The spectra of the remaining records are whitened by dividing the amplitude of the noise
190 spectrum by its absolute value between 0.5 and 80 s without changing the phase. (5) To
191 ensure that small earthquake signals are generally removed, we perform a second and more
192 standard clipping of the resulting waveforms at 4 standard deviations of the amplitudes. (6)
193 The data are down-sampled to 4 Hz to reduce the size of the files. (7) Finally, we compute the
194 cross correlations between the corresponding segments at two different stations in the
195 frequency domain as in Bensen et al. (2007). The correlation function for each day is the
196 average of the segments remaining after the above pre-processing in that day. As most of our
197 stations record 3 components signals, we compute the 9 inter-component (vertical (Z), North-
198 South (N) and East-West (E)) correlations functions corresponding to the elastic Green's
199 tensor (ZZ, ZE, ZN, EZ, EE, EN, NZ, NE, NN). This correlation tensor is then rotated along
200 the inter-station azimuth to provide the correlation functions between the radial (R),
201 transverse (T) and vertical (Z) components (RR, RT, RZ, TR, TT, TZ, ZR, ZT, ZZ) of the
202 seismic wavefield propagating directly along the great circle connecting the two stations.

203 The main purpose of this pre-processing procedure (Poli et al., 2012) is to remove as
204 many as possible transient sources from the noise data. Figures S1 and S2 illustrate the
205 improvement in the surface wave reconstruction (e.g., signal to noise ratios, reasonable
206 arrivals on positive and negative times, dispersion) compared to usual methods based on
207 whitening and cutting the traces according to a pre-determined threshold (Bensen et al., 2007;
208 Shelly et al., 2009, Hillers et al., 2013). Figure S1a presents a day of data with an earthquake
209 and Figure S1b shows a corresponding waveform where a classical clipping (here at 4
210 standard deviations) was used to clean the time series. With such standard clipping, the
211 earthquake signal is not fully removed from the data. This is better shown on Figure S2a that
212 compares the cross correlation for that particular "earthquake day" (red trace) and a reference
213 day (blue trace) without a visible earthquake. The correlation function for the earthquake day
214 is different from the one obtained with the cleaner noise wave field. In the former case,
215 surface waves are masked due to the earthquake signals that produce a high amplitude
216 localized pulse that dominates the noise scattered wave field. With the modified Poli et al.
217 (2012) procedure employed here, the last segment with the earthquake is removed (Figure

218 S1c). The correlation function computed after this treatment (red trace in Figure S2b) is
219 considerably improved, with clear arrivals in both positive and negative time as in the
220 reference noise day (blue trace), compared to the results in Figure S2a.

3.2. Surface waves reconstruction and noise directionality

223 Figure 2a and 2d show examples of ZZ daily correlations functions, presented as
224 correlograms for different Julian days in 2012, between stations PLM-PSD (left) and stations
225 PER-BOR (right). We choose these pairs of stations (see Figure 1 for station locations) to
226 illustrate two particular propagation directions: the paths between PLM-PSD and PER-BOR
227 are, respectively, normal and parallel to the coast (which is the largest source of noise) and the
228 SJFZ. Both correlograms show clear and stable arrivals at positive and negative times for the
229 entire year (the asymmetry of the correlation functions observed for PLM-PSD and the
230 reduced amplitudes for PER-BOR are discussed below). The temporal stability of the daily
231 correlations indicates that most of the transient sources have been properly removed from the
232 traces by the pre-processing method describe above, leading to stable arrivals in the
233 correlation functions associated with the seismic wavefield propagating between the two
234 stations.

235 The daily correlations have 5-10% amplitude variations without clear seasonal evolution,
236 which may affect the quality of the cross correlations by reducing the SNR for particular days
237 leading to less accurate travel times measurements. We remove these small-scale variations
238 and increase the overall SNR by stacking the daily correlation functions for the whole year
239 2012 to obtain average ZZ correlations (top traces in Figures 2b and 2e). Similar analyses
240 give the average inter-component correlations between the vertical and radial (ZZ, ZR, RZ,
241 RR) and transverse (TT) components (Figures 2b and 2e). The arrival patterns observed for
242 all correlation components in both the positive and negative times are dominated by surface
243 waves travelling between the used pairs of stations. In both examples, the ZZ, ZR, RZ and RR
244 terms have Rayleigh waves that show similar group time delays for all traces, and the
245 expected phase shift due to the elliptical polarization of Rayleigh waves between the ZZ and
246 RZ correlations. The TT correlations have Love waves.

247 Figure 2c and 2f present period-group velocity diagrams resulting from the combination
248 of the ZZ, ZR, RZ and RR components with a logarithm stacking method describe in section

249 4.1. A clear dispersive pattern corresponding to the fundamental Rayleigh wave mode is
1 250 observed in both cases for periods between 3 and 12s. The dispersion curves extracted from
2 251 these period-group velocity diagrams (black lines on Figure 2c and 2f) show different
3 252 dispersion characteristics between the two paths (e.g., higher Rayleigh wave group velocities
4 253 for PER-BOR compare to PLM-PSD, and more stable Rayleigh dispersion for PLM-PSD
5 254 with a slightly increasing group velocity for increasing period) that reflect the different media
6 255 sampled by the reconstructed Rayleigh waves travelling between PLM-PSD and PER-BOR.

13 256 Clear differences in term of amplitudes and symmetry are observed for the two
14 257 propagation directions plotted in Figure 2. The correlations for coast-normal directions (left
15 258 panels) show an asymmetric surface wave amplitude pattern, while the coast-parallel
16 259 directions present (right panels) more symmetric correlations functions with reduced
17 260 amplitudes. This is explained by the dominance of near-coastal excitation of the noise field in
18 261 southern California and scattering mean free path that is too short to completely randomize
19 262 the ambient noise (Hillers et al., 2013). As a result, the amplitudes of the reconstructed
20 263 surfaces waves are significantly higher for the west-east propagation direction corresponding
21 264 to the noise directionality between PLM and PMD. The lack of strong noise sources for coast
22 265 parallel directions explain the symmetry and overall amplitude reduction of the reconstructed
23 266 surfaces waves between PER and BOR. The non-isotropic distribution of noise sources may
24 267 bias (e.g. Weaver et al., 2009; Froment et al., 2010) the measured travel times on correlation
25 268 functions Hillers et al. (2013) studied the potential errors on arrival-time measurements of
26 269 Rayleigh waves in the SJFZ region due to the directional noise and found the effect to be
27 270 small. We note that the strong directional distribution of noise sources will mainly affect the
28 271 coast-normal paths (Figure 2). The distribution of 158 stations used in thsi work (Figure 1)
29 272 leads a large number of paths in all directions that helps obtaining reliable results on surface
30 273 wave propagation in the region.

33 274 Figure 3 illustrates the propagation of the surfaces waves through the entire network, by
34 275 showing the 9 components of the correlation tensor as a function of the inter-station distances.
35 276 The correlations are stacked in 0.5 km distance bins for a better visualization. As in the 2
36 277 specific station pairs used for the examples in Figure 2, prominent Rayleigh waves are
37 278 reconstructed on the RR, ZZ, RZ and ZR components and Love waves are reconstructed on
38 279 the TT correlation term. The remaining transverse components (RT, TR, TZ, ZT) show only
39 280 weak diffuse phases, as expected theoretically, lending support to the quality of the rotations
40 281 along the inter-station azimuth (see section 3.1). In the following sections we perform travel

282 times measurements on the various components and use the data to obtain tomographic
283 images for the region.

284

285 4. SURFACE WAVE TOMOGRAPHY

286 In this section, we use Rayleigh and Love waves constructed from the ambient noise cross
287 correlation to image the shallow crust in the southern California plate-boundary region. We
288 derive dispersion curves for all station pairs, after which we invert the dispersion curves first
289 for group velocities and then shear wave velocity maps for the region.

291 *4.1 Dispersion measurements and paths selection*

292 The dispersion measurements are done for periods of 1 to 25 sec from the reconstructed
293 surface waves using the frequency-time analysis (FTA) of Levshin et al. (1989). The
294 dispersion analysis can be done on both the causal and anti-causal parts of the correlations.
295 For Rayleigh waves, we take advantage of the 4 components of the correlation tensor (RR,
296 ZZ, RZ, ZR) that contain Rayleigh waves. We first compute the FTA for each signal i
297 independently to obtain a normalized period-group velocity diagram $N_i(T,u)$, where T is the
298 period and u the group velocity. The results are then combined with a logarithmic stacking
299 method in the period-group velocity domain as in Campillo et al. (1996)

$$300 \quad A_s(T,u) = \prod_i N_i(T,u), \quad 1)$$

301 where $A_s(T,u)$ is the combined period-group velocity diagram on which the dispersions are
302 calculated. The width of the mean envelope at a given period is proportional to the inverse of
303 the number i of the stacked FTA (8 in our case), and its amplitude depends on the standard
304 deviation of the group velocities. The dispersion measurements are evaluated on the
305 $[A_s(T,u)]^{(1/i)}$ diagram, which provides amplitude values between 0 and 1 independently of the
306 number i of stacked FTA. We use only the period-group velocity region on the $[A_s(T,u)]^{(1/i)}$
307 diagram for each pair of stations that have maximum amplitude above 0.3. The same method
308 is used to extract Love wave dispersion curves, using in that case only the two possible
309 measurements (on the causal and anti-causal TT correlation). Given the different amounts of

310 measurements, we expect generally more reliable results for Rayleigh waves than for Love
311 waves.

312 This technique is used on data with sufficiently high SNR on both the causal and anti-causal
313 parts of the correlation functions (Figure 3), including paths with strongly asymmetric noise
314 sources (e.g., left panels of Figure 2). Moreover, the logarithmic stacking method takes
315 advantage of different frequency contents in the opposite propagation directions for some
316 pairs of station. Due to the dominant near coastal excitations, the incident noise direction
317 coming from the Pacific includes higher frequencies compare to the opposite direction
318 (Hillers et al., 2013). As illustrated in Figures 2c and 2f, using combinations of the ZZ, ZR,
319 RZ and RR measurements on the positive and negative times, we obtain clear Rayleigh wave
320 dispersion curves both for coast-normal and -parallel paths. If the measurements obtained
321 from the opposite incident noise directions are not sufficiently similar, the resulting stacked
322 period-group velocity diagram will not reach the threshold (here 0.3) to be considered in the
323 tomography.

324 Figure 4 shows histograms of the measured group velocity for Rayleigh (Fig. 4a) and
325 Love (Fig. 4b) waves at a period of 7 sec for all pairs of stations. For Rayleigh waves, the
326 measured velocity has a mean value of 2.86 km/s with a relatively symmetric spread
327 associated with standard deviation of 0.39 km/s. For Love waves, the average velocity is 2.92
328 km/s with a more asymmetric spread and standard deviation of 0.45 km/s. The relatively large
329 standard deviations are expected in the Southern California study region with strong lateral
330 variations of velocities (Allam and Ben-Zion, 2012). The more disordered results for Love
331 waves compared to Rayleigh waves are expected from the smaller number of measurements.
332 To increase the quality of the inversions, we require the measurements to satisfy 3 different
333 criteria. First, we remove all correlation functions with a SNR under 7 to ensure that the travel
334 times are well estimated. Second, for each measured period we exclude all paths with a length
335 smaller than one wavelength. Due to the size of the area under investigation, we have small
336 number of paths for period above 12s (Table 1). Given this and our interest in the shallow
337 crust, we focus on periods below 12s. Finally, we keep only the velocity measurements in a
338 range of two standard deviations from the mean (red vertical lines in Figures 4a,b). This
339 reduces the variability in the measurements and avoids unrealistic values for the inversion.
340 Table 1 summarizes the number of selected measurements at each period used in the
341 inversions.

342

1

2

3

4

5

6

7

8

9

10

11

12

13

14

15

16

17

18

19

20

21

22

23

24

25

26

27

28

29

30

31

32

33

34

35

36

37

38

39

40

41

42

43

44

45

46

47

48

49

50

51

52

53

54

55

56

57

58

59

60

61

62

63

64

65

4.2 Azimuthal Anisotropy

Before inverting the data for isotropic velocity models, we analyze potential azimuthal anisotropy in the high-quality velocity measurements satisfying the criteria discussed above. This can augment the isotropic velocity models by providing information on the orientation of velocity variations in the southern California plate boundary area. Numerous studies demonstrated the existence of seismic anisotropy in the shallow crust around fault zones from shear wave splitting in earthquake waveforms (e.g., Aster et al. 1990; Peng and Ben-Zion 2004; Liu et al. 2005; Boness and Zoback 2006; Yang et al. 2011). As the noise correlations are dominated by the fundamental mode of surface waves, we can use the selected group velocity measurements obtained from the cross correlations to infer on azimuthal anisotropy in the SJFZ region (e.g., Lin et al., 2009, 2011; Fry et al., 2010; Mordret et al., 2013b). The use of dispersive surface waves, which are sensitive to deeper structures for increasing periods, may be used to retrieve the 3D distribution of azimuthal anisotropy.

Figures 5a and 5b display the azimuthal distribution of the group velocity measurements (Figure 4) at 7 s for Rayleigh and Love waves (small black dots). The large red dots with error bars are group velocities averaged over 10° bins. The results exhibit an azimuthal dependence of values, with azimuths around 10° and 200° showing significantly higher velocities for both Rayleigh and Love waves. To study the azimuthal distribution, we use a parameterization similar to Smith and Dahlen (1973). For a slightly anisotropic medium, the group velocities can be approximated in the form of an even order harmonic function with 180° (2θ anisotropy) and 90° (4θ anisotropy) periodicity:

$$U(\theta) = u_0 + A \cdot \cos(2(\theta - \varphi_2)) + B \cdot \cos(4(\theta - \varphi_4)), \quad (2)$$

where u_0 is the average group velocity, θ is the azimuth, A and B are peak-to-peak relative amplitudes of the 2θ and 4θ terms, and φ_2 and φ_4 define the orientation of the fast axes for the 2θ and 4θ terms. The blue lines in Figs 5a and 5b show the optimal fit. The results indicate 2θ azimuthal anisotropy of 6-10% for incident propagation directions oriented around 200° (Figs 5c and 5d). The 4θ component is only a few percent and has maximum speed oriented in the same direction. We note that group velocities extracted from Love waves show a higher (by about 4% to 5%) 2θ anisotropy, which may reflect less reliable velocities based on only two independent measurements. The amplitudes and orientations found for both the average 2θ

373 and 40 terms are in general agreement with previous studies (e.g. Moschetti et al., 2010; Lin
1 374 et al., 2011; Ritzwoller et al., 2011). The origin of this average azimuthal anisotropy is not
2 375 fully clear. One possible explanation is a bias due to the strongly asymmetric noise sources
3 376 concentrated at the Pacific (e.g., Hillers et al. (2013) and section 3.2), which correspond to the
4 377 fast direction angle around 200° (Fig. 5d). A good test of this potential bias is to invert for the
5 378 spatial distribution of the azimuthal anisotropy. If the strong directionality of noise sources
6 379 biases the measurements we expect to find a coast perpendicular fast direction for the entire
7 380 map. In contrast, if the fast directions are affected by prominent structures (e.g. fault zones,
8 381 basins) this will suggest a physical origin related to the crustal properties.

16
17 382 To reduce the uncertainties, we combine all measurements within 8 km x 8 km cells (Lin
18 383 et al., 2009; Mordret et al., 2013b). The results in each cell are averaged on 20° azimuth bins
19 384 and fitted by equation (2). We define the misfit of the inversion at a single cell as the standard
20 385 deviation between the measured and predicted group velocities (Mordret et al., 2013b) and
21 386 use for interpretation only the cells with a misfit smaller than 0.15 km/s. Figure 6 presents the
22 387 resulting maps for the Rayleigh and Love waves. As found in previous studies (e.g. Lin et al.,
23 388 2011; Ritzwoller et al., 2011), we observe clear spatial variations with overall correlation
24 389 between the 2θ fast direction orientation and major geological structures. Lin et al. (2011)
25 390 used both noise correlations and earthquake data and found the same pattern of azimuthal
26 391 anisotropy with fast directions that follow the main geological boundaries in southern
27 392 California. The results of Figure 6 provide additional details to the large scale analysis of Lin
28 393 et al. (2011). The fast directions are generally aligned with the system of strike-slip faults that
29 394 make the southern California plate boundary region, with some deviations related to structural
30 395 complexities. The region where the SJFZ and SAF are merging and other places with major
31 396 fault branches show rotations of fast directions. Around the Anza section of the SJFZ with
32 397 relatively simple geometry, the degree of azimuthal anisotropy is considerably smaller than in
33 398 structurally complex regions. The coast-perpendicular fast directions may be associated with
34 399 rotations in areas with multiple complex structures, or reflect in some places artifacts related
35 400 to the directionality of the noise sources.

53 401 54 55 402 *4.3. Inversion of dispersion measurements for group velocities*

56
57
58
59
60
61
62
63
64
65

403 The dispersion measurements are inverted to obtain isotropic group velocity maps
 404 following the Barmin et al. (2001) method. The standard forward problem is written in tensor
 405 notation as:

$$d = Gm, \quad (3)$$

407 where $d = t^{means} - t^0$ is the data vector consisting of the differences between the measured group
 408 traveltimes and those computed with the initial model for each path. The matrix G represents
 409 the surface wave traveltimes for each path in each cell of the initial model. The inversion
 410 target is the group velocity map $m = (u - u_0)/u_0$, where u is the velocity obtained after inversion
 411 and u_0 the initial group velocity. For each period, the initial model over the entire region is the
 412 average value of all the measurements at that period.

413 The Barmin et al. (2001) inversion is based on minimization of a penalty function having
 414 a linear combination of data misfits, magnitude of perturbation and model smoothness:

$$(G(m) - d)^T (G(m) - d) + \alpha^2 \|F(m)\|^2 + \beta^2 \|H(m)\|^2, \quad (4)$$

415 where F is a Gaussian spatial smoothing function with correlation length σ written as:

$$F(m) = m(r) - \int_s \exp\left(-\frac{|r - r'|^2}{2\sigma^2}\right) \cdot m(r') dr' \quad (5)$$

416 The last term H is defined as:

$$H(m) = \exp(-\lambda\rho) \cdot m, \quad (6)$$

417 where ρ is the path density (discussed further and illustrated in section 4.4 below) and λ a
 418 weight parameter that produces gradual fading of the inverted model into the initial model in
 419 areas where the path density is low.

420 Four parameters are used to regularize the solution: the magnitude of model perturbations
 421 is controlled by β and λ , set here to 3 and 0.4, while the spatial smoothing is controlled by α
 422 and σ . The correlation length σ is set at 3 km, which is double of the cells size, and the weight
 423 α given to the spatial smoothing term of the misfit function in equations (4) and (5) is fixed
 424 through a standard L-curve analysis by plotting the variance reduction as a function of α . The
 425 preferred value of α (15) is chosen to be near the maximum curvature of the L-curve. Note
 426 that β and λ influence the model only for cells with low path coverage. With high path density

430 the smoothing is mainly controlled by α and σ . In the following, we focus only on cells with
431 high path coverage where β and λ have little influence.

432 Figure 7 gives inverted group velocity maps at 3s, 5s, 7s and 9s for Rayleigh waves and
433 Figure 8 provides corresponding maps for Love waves. The results show overall increasing
434 velocities with periods associated with the dispersion of the Rayleigh and Love waves. In
435 addition, the images reflect a diversity of structural features including clear velocity contrasts
436 across the main faults along with low velocity damage zones and basins. The low velocity
437 damage zones are especially pronounced at low periods of Love waves in areas of structural
438 complexity (e.g. the trifurcation area and region between the SAF and SJFZ); the low velocity
439 zone around the Salton trough persists up to 9 s. The NE block of the SJFZ has higher group
440 velocities than the SW block at periods up to 5 s, other than in the region between the SJFZ
441 and SAF to the NW of the San Jacinto basin (see Figure 1) where the SW block has higher
442 velocities. At periods longer than 5 s, the velocity contrast along the central SJFZ is small,
443 while to the NW of the San Jacinto basin the SW block has higher group velocities. The
444 group velocity maps also show a clear contrast across the southern SAF near the Salton
445 trough that produces a slower SW block, and across portion of the Elsinore fault with faster
446 SW block up to periods of 7 s.

448 **4.4. Inversion resolution**

449 The resolution of the inversion with the Barmin et al. (2001) method is described by a
450 resolution matrix that depends mostly on the network geometry and distribution of high-
451 quality measurements that satisfy the criteria discussed in section 3. The rows of the
452 resolution matrix give the resolution of the final model at each cell by quantifying the
453 dependency of the obtained group velocity at that location to the measurements at all other
454 locations. The quality of the obtained maps can be assessed using (1) the path density in each
455 cell, and (2) the resolution length at each node defined as the distance for which the value in
456 the resolution matrix has decreased by a factor of 2. Figures 9a and 9b show the path density
457 in each cell of 1.5km^2 for the obtained Rayleigh and Love waves at 7s. The path coverage in
458 the region of interest from the Elsinore fault to the SAF is good with more than 20 paths per
459 cell. Close to the SJFZ, the path coverage increases to a minimum of 40 paths per cell with a
460 maximum value of 164 paths. The only poorly resolved region is SE of the trifurcation area
461 where the number of paths decreases rapidly due to the lack of stations in that region. Figures

462 9c and 9d present the correlation length in each model cell. There is good (relatively small)
1 463 correlation lengths in the range 2-4 km in most of the region around the SJFZ, up to the SAF
2 464 to the NE and the Elsinore fault to the SW. The resolution in the Salton Sea region is reduced
3 465 with correlation length above 7km, and is poor to the SE of the trifurcation area due to lack of
4 466 data in that area. We also note that the path coverage is lower and the correlation length
5 467 higher for Love waves due to results at less cells compared with Rayleigh waves (see Figures
6 468 7 and 8), which is related to the smaller number of measurements used to reconstruct the Love
7 469 waves.

18 471 **5. INVERSIONS FOR 3D SHEAR-WAVE VELOCITIES**

21 472 *5.1 Inversion method and resolution*

23 473 In this section we use the linearized inversion scheme of Hermann & Ammon (2002) to
24 474 invert the obtained group velocity maps at each period for shear wave velocities. Considering
25 475 the period interval from 3s to 12s for which we have reliable group velocity maps, we focus
26 476 the inversion on the top 5-7 km of the crust. This is an important depth range since the
27 477 velocities structure in the top few km of the SJFZ area are not well constrained by earthquake
28 478 topography (Allam & Ben-Zion 2012). We first invert for an average depth-dependent V_s
29 479 model and then use the local dispersion curves extracted from the group velocity maps to
30 480 obtain depth-dependent V_s profiles at each cell of the grid. By combining all local 1-D
31 481 profiles we obtain a detailed 3-D shear wave velocity structure in the study region.

41 482 The quality of the inverted models with the linear approach of Hermann & Ammon
42 483 (2002) depends on the accuracy of the initial model. To have an good initial model we use the
43 484 results from the double-difference earthquake topography of Allam and Ben-Zion (2012),
44 485 which provide detailed images of crustal velocities over the depth range ~3-15 km. We begin
45 486 with a starting model that consists of laterally-average velocities from Allam & Ben-Zion
46 487 (2012) in 60 layers with thickness values that vary from 500 meters for the first 40 layers to 1
47 488 km for the others (Figure 10a). With the limited depth resolution of the fundamental mode of
48 489 Rayleigh and Love waves for the considered periods, we impose smooth velocity variations
49 490 with depth in the top 30 layers. The velocity is allowed to take a large range of values as long
50 491 as the depth variation is smooth. The obtained models are well-defined solutions given the
51 492 model parameterization as discussed below.

493 Using the above initial model, we invert the average group velocity dispersion curves
494 (Figures 10b and 10c) to obtain related average crustal V_s models for the region (Figure 10a).
495 We compute the average dispersion curves by averaging the group velocity maps at each
496 period in cells with path density above 5. Figures 10b and 10c show the average group
497 velocity curves, along with theoretical dispersion curves associated with the inverted
498 Rayleigh- and Love-based models of Figure 10a. As shown in Figure 10d, the results are well
499 fitted with a misfit of less than 0.01 km/s for both Rayleigh and Love waves. The depth
500 resolution of the inversions of the data in the 3-12 s periods is relatively high over the shallow
501 crust for both Rayleigh and Love waves. The resolution matrices presented in Figures 10e and
502 10f indicate good resolution up to 7-10 km for Rayleigh waves and up to 5-7 km for Love
503 waves. The V_s model based on the Love waves shows higher velocities by about 6% in the
504 shallow structures (Figure 10a). This may stem from a combination of less reliable Love wave
505 group velocities measurements and/or azimuthal anisotropy. The path coverage, which is
506 limited for Love waves on the model edges where low velocity zones associated to the SAF
507 and Elsinore fault are observed, may also explain the differences between the Rayleigh and
508 Love waves results.

509 To improve the inversion results, we proceed by inverting V_s at each grid cell starting
510 from the local high-resolution model of Allam & Ben-Zion (2012). For cells not covered by
511 that model we use the average depth-dependent results as above. The data misfit over all cells
512 and periods are small being generally bellow ± 0.05 km/s for Rayleigh waves (Figure 10g).
513 The inversions of the Love group velocity maps have slightly higher misfits on the order of
514 ± 0.1 km/s (Figure 10h). As the misfit values are close to the errors of the dispersion
515 measurements, the obtained results are well defined for the range of used periods.

5.2 V_s maps and profiles

518 Figures 11 and 12 show, respectively, map views of the V_s values derived at various
519 depths from the group velocities of the Rayleigh and Love waves. As in Figures 7 and 8, we
520 observe complex structures that include multiple features of interest. The SJFZ is well marked
521 with low velocity zones and velocity contrasts across the fault. In the section to the SE of the
522 San Jacinto basin the NE block has higher V_s values, and the sense of velocity contrast is
523 reserved across the section between the San Jacinto basin and the SAF. Velocity contrasts are
524 also observed across the southern part of the SAF and the southern section of the Elsinore

525 fault, with a faster SW block in both cases. Both the SAF and SJFZ have prominent low
1 526 velocity zones in the top 5 km in areas of structural complexities, that extend to 7 km in the
2 527 region between the two faults and the Salton trough area. Another interesting low velocity
3 528 zone extends near the SE edge of the model from the trifurcation area of the SJFZ toward the
4 529 Elsinore fault. This feature is very pronounced at 1-3 km in the maps based on both Rayleigh
5 530 and Love waves (Figures 11 and 12). At depth of 7 km, the most pronounced features in the
6 531 results based on Rayleigh waves are the low velocity zones between the SAF and SJFZ and
7 532 SW of the SAF close to the Salton trough (Figure 11d). In general, the tomographic images
8 533 from the Rayleigh and Love waves have very consistent results on the complex structure
9 534 plate-boundary region in the top 5 km. Some of the discussed features are better shown in the
10 535 fault-normal cross-section presented in Figures 13 and 14.

11 536 Figure 13 and 14 show Vs images based on Rayleigh and Love waves, respectively, on
12 537 the fault-normal cross-sections marked as profiles 1 to 7 in Figure 1. Profiles 1-4 go through
13 538 the complex damaged region between the SAF and SJFZ and exhibit low velocities in the top
14 539 2-4 km that are primarily on the NE side of the SJFZ. Profiles 2-4 show a strong velocity
15 540 contrast across the SJFZ that coincides with the surface trace of the fault. The velocities to the
16 541 NE at these locations are reduced by up to 40% in the top 4 km of the crust. As shown in
17 542 Figure 1, the region between the SAF and SJFZ has high seismicity that is broadly distributed
18 543 with hypocentral depths between 4km to 20km (Hauksson et al., 2012). We therefore observe
19 544 spatial correlation between strong shear wave velocity reduction at shallow depths and
20 545 seismicity at seismogenic depth. Profiles 5-6 show the influence of the San Jacinto Basin that
21 546 reduces Vs strongly in the top 2 km on both sides of the main surface trace (Clark fault).
22 547 Profile 7 crosses the trifurcation point and shows LVZ in the top 2 km both sides of the Clark
23 548 fault. The entire trifurcation area is associated with high seismicity (Figure 1) showing again a
24 549 spatial correlation between shear wave velocity reduction in the top few km and the seismicity
25 550 at depth. The widths of the LVZ are decreasing with depth especially in the images associated
26 551 with Love waves (Figure 14), leading to flower shape structures.

27 552 The results obtained from the Love wave dispersion curves are generally in agreement
28 553 with the Rayleigh wave based results. Most of the observed features with both wave types
29 554 (low velocity fault damage zones, velocity contrasts and basin effects) are consistent. The
30 555 overall lower resolution of the Love wave leads to more diffuse Vs images. As discussed for
31 556 the average model, the shear wave velocities are usually higher by a few percent for the Love
32 557 waves. However, the velocity reductions near basins or fault zones at shallow depth (1-3 km)

558 are stronger for the Love wave inversions. This may stem from the higher sensitivity of Love
1 559 waves to shallow structures; they are more affected by the damage zones and basins in the
2
3 560 first few kilometer of the crust in the region.
4
5

6. DISCUSSION AND CONCLUSIONS

6 561
7
8
9 562
10
11 563 We performed detailed imaging of the seismic velocity structure in the top 5-7 km of the
12
13 564 plate boundary region in southern California using noise-based Rayleigh and Love waves.
14
15 565 The results complement earthquake tomography studies in the region (e.g., Hauksson, 2000;
16
17 566 Lin et al. 2007; Allam and Ben-Zion 2012), which have low resolution in the top 2-3 km and
18
19 567 in horizontal sections not covered well by propagation paths associated with earthquakes. To
20
21 568 first order, the observed velocity structures are correlated with the surface geology, showing
22
23 569 higher Vs in plutonic rocks (Sharp, 1967) such as the Thomas Mountain Pluton on the NE
24
25 570 block of the SJFZ near Anza. Our tomographic images show various additional fault zone
26
27 571 features (velocity contrasts, damage zones, basins, anisotropy) that are generally in good
28
29 572 agreement with the detailed earthquake tomography studies of the SJFZ environment (Allam
30
31 573 and Ben-Zion 2012; Allam et al. 2014) and larger scale imaging with earthquake and noise
32
33 574 data (Tape et al. 2010; Ritzwoller et al. 2011; Lin et al., 2011).
34

35 575 The dispersion measurements of the Rayleigh and Love waves indicate (Figures 5-6) the
36
37 576 existence of 2 θ azimuthal anisotropy, which is about 6-10% at 7s period, with overall coast-
38
39 577 perpendicular fast directions (around 200°). The results are consistent generally with large
40
41 578 scale anisotropy studies in the region (e.g., Lin et al., 2011; Alvizuri and Tanimoto, 2011),
42
43 579 and show additional smaller scale features correlated with various elements of fault structures.
44
45 580 The fast directions tend to align with the direction of the main strike-slip faults, but exhibit
46
47 581 strong rotations near major complexities such as the trifurcation area and the region between
48
49 582 the SJFZ and SAF. On the geometrically simpler Anza section of the SJFZ there is a
50
51 583 reduction of azimuthal anisotropy. Some aspects of the derived azimuthal anisotropy may be
52
53 584 affected by the strong directionality of the noise sources in the area (e.g., Schulte-Pelkum et
54
55 585 al. 2004; Hillers et al. 2013). However, the correlations between spatial variations of the
56
57 586 observed azimuthal anisotropy and various structural features suggest an overall physical
58
59 587 origin of the discussed results, involving fault-parallel shearing and various perturbations near
60
61 588 major fault complexities.
62
63
64
65

589 The obtained images of shear wave velocities show clear velocity contrasts across the
1 590 SJFZ and Ellsinore fault, along with low velocity zones along the SJFZ and SAF that are
2 591 especially pronounced in the region between the two faults, around the San Jacinto basin and
3 592 trifurcation area of the SJFZ, and in the Salton trough area (Figures 11-15). Shallow low
4 593 velocity zones also appear to extend from the SJFZ toward the Elsinore fault in the top 1-2
5 594 km. For the 3-7 km depth range where both our study and the Allam and Ben-Zion (2012)
6 595 tomography provide reliable images, there is good agreement in the locations of the velocity
7 596 reductions associated with basins and damage zones, although their lateral extent is larger in
8 597 our study due to the larger employed near-fault grid size. However, as shown by the average
9 598 model in Figure 10a, our results are generally slower by about 2-10% at different depths than
10 599 those of Allam & Ben-Zion (2012). The differences between the two models decrease with
11 600 increasing depth, suggesting that the different depth resolution of both studies may explain
12 601 the discrepancy. The earthquake tomography has good resolution from about 3 km to about
13 602 15km (Allam and Ben-Zion, 2012), while our noise-based surface waves imaging with
14 603 periods between 3 and 12 seconds is mostly sensitive to the first 5 to 8 km of the crust. The
15 604 resolution of the earthquake tomography decreases rapidly below 3 km due to the almost
16 605 vertical ray paths, so the inversion results of Allam and Ben-Zion (2012) for the shallow crust
17 606 are likely influenced (overestimated) by the deeper structures. Similarly, our inversion results
18 607 likely project shallower structures somewhat deeper leading to underestimated velocities.
19 608 Systematic sensitivity studies of both inversion methods to depth is needed to understand
20 609 better the generally slower V_s values obtained in our analysis.

39 610 Our noise-based tomography allows us to image velocity contrasts across various fault
40 611 sections (Figures 13-14) and flower-shape damage zones (Figure 15) essentially up to the
41 612 surface. We observe higher V_s values on the NE block of the central section of the fault to the
42 613 SE of the San Jacinto basin, and a reversed contrast between the San Jacinto basin and the
43 614 SAF. Similar contrasts were observed over the seismogenic sections of the SJFZ by Allam
44 615 and Ben-Zion (2012) and Allam et al. (2014). As discussed in those paper, the observed
45 616 velocity contrasts combined with model results on bimaterial ruptures (e.g., Ben-Zion and
46 617 Andrews 1998; Shi and Ben-Zion 2006; Ampuero and Ben-Zion 2008) imply a statistically
47 618 preferred rupture direction of earthquakes on the central section of the SJFZ to the NW. This
48 619 inference is consistent with observed rock damage asymmetry across the fault (Dor et al.,
49 620 2006; Lewis et al., 2005; Wechsler et al., 2009), along-strike asymmetry of aftershocks
50 621 (Zaliapin and Ben-Zion 2011), and reversed-polarity secondary deformation structures near

622 segment ends (Ben-Zion et al., 2012). The reserved velocity contrast NW of the San Jacinto
1 623 basin may act as a dynamic barrier for NW propagating ruptures that nucleate around Anza or
2 624 in the trifurcation area. We also observe a clear velocity contrast across the SE part of the
3 625 Elsinore fault with higher Vs on the SW side, and little or possibly reversed contrast on the
4 626 NW section of the fault. The validity of these results for the deeper sections of the Elsinore
5 627 fault should be substantiated with detailed earthquake tomography or noise imaging using
6
7 628 longer periods.

13 629 The flower-shape damage zones around the SJFZ and SAF in Figure 15, with broader
14 630 damage around geometrical fault zone complexities, merge nicely with the images of Allam
15 631 and Ben-Zion (2012) and are consistent with theoretical results on decreasing damage width
16 632 with depth (e.g. Ben-Zion and Shi 2005; Finzi et al. 2009; Kaneko and Fialko 2011). It is
17 633 interesting to note that the broad damage zone in the region between the SJFZ and SAF, with
18 634 up to 40% velocity reduction in the top few km, corresponds to a zone of high and diffuse
19 635 seismicity at seismogenic depth (Hauksson et al., 2012). A similar correlation between
20 636 significant broad shallow damage zone and deep diffuse seismicity is also observed in the
21 637 complex trifurcation area that is associated with highly heterogeneous focal mechanisms
22 638 (Bailey et al., 2010; Hauksson et al., 2012). The broad damage zones are generally relic
23 639 structures reflecting the early organizational stage of the fault zone (e.g. Ben-Zion and
24 640 Sammis, 2003). The correlations of such zones with the diffuse seismicity can be explained
25 641 by remaining geometrical heterogeneities that persist at seismogenic depth and produce local
26 642 stress concentration that initiate ruptures.

39 643 The noise-based tomographic results of this paper improve significantly the available
40 644 information on the seismic velocities in the top 5-7 km of the complex plate boundary region
41 645 around the SJFZ. More detailed imaging of the velocity structure in the top 500 m or so may
42 646 be obtained using correlations of coda waves (e.g., Campillo and Paul, 2003) or correlations
43 647 of full earthquake waveforms (Roux and Ben-Zion 2014). Integrating the imaging results
44 648 associated with the available earthquake and noise data is best done by performing joint
45 649 inversions of the different measurements. This will be done in a follow up work.

56 651 **Acknowledgments**

58 652 The data used in this work were recorded mostly by the Southern California Seismic
59 653 Network operated by Caltech and USGS. We also used data recorded near the SJFZ by a

654 temporary NSF-CD deployment operated by the University of California, San Diego, and data
1 655 recorded by the University of California, Santa Barbara. We thank Amir Allam, Gregor
2 656 Hillers, Nikolai Shapiro, Laurent Stehly and Frank Vernon for useful discussions. The study
3 657 was supported by the National Science Foundation (grant EAR-0908903).
4
5
6
7 658
8
9

10 659 REFERENCES

- 11
12 660 Allam, A. A., and Y. Ben-Zion (2012), Seismic velocity structures in the Southern California
13 661 plate-boundary environment from double-difference tomography, *Geophys. J. Int.*, 190,
14 662 1181–1196, doi:10.1111/j.1365-246X.2012.05544.x.
15
16 663 Allam, A. A., Y. Ben-Zion I. Kurzon and F. L. Vernon (2014), Seismic velocity structure in
17 664 the Hot Springs and Trifurcation Seismicity Cluster Areas of the San Jacinto Fault Zone
18 665 from double-difference tomography, *Geophys. J. Int.*, in review.
19
20
21 666 Alvizuri, C., and T. Tanimoto, (2011). Azimuthal anisotropy from array analysis of Rayleigh
22 667 waves in Southern California. *Geophys. J. Int.*, 186, B08307.
23
24 668 Ampuero, J.-P. and Ben-Zion, Y., (2008). Cracks, pulses and macroscopic asymmetry of
25 669 dynamic rupture on a bimaterial interface with velocity- weakening friction, *Geophys. J.*
26 670 *Int.*, 173, 674–692, doi:10.1111/j.1365-246X.2008.03736.x.
27
28
29 671 Aster, R.C., Shearer, P.M. & Berger, J., 1990. Quantitative measurements of shear wave
30 672 polarizations at the Anza seismic network, southern California: Implications for shear
31 673 wave splitting and earthquake prediction, *J. Geophys. Res.*, 95, 12 449–12 473.
32
33 674 Bailey, I. W., Ben-Zion, Y., Becker, T. W. and Holschneider, M. (2010), Quantifying focal
34 675 mechanism heterogeneity for fault zones in central and southern California. *Geophysical*
35 676 *Journal International*, 183: 433–450. doi: 10.1111/j.1365-246X.2010.04745.x
36
37
38 677 Barmin, M., M. Ritzwoller, and A. Levshin (2001), A fast and reliable method for surface
39 678 wave tomography, *Pure Appl. Geophys.*, 158(8), 1351–1375.
40
41 679 Bensen G.D., Ritzwoller M.H., Barmin M.P., Levshin A. L., Lin F., Moschetti M. P, Shapiro
42 680 N. M. Yang Y., (2007), Processing seismic ambient noise data to obtain reliable broad-
43 681 band surface wave dispersion measurement, *Geophys. J. Int.*, 169, 1239–1260.
44
45
46 682 Ben-Zion, Y., (2008). Collective behavior of earthquakes and faults: continuum-discrete
47 683 transitions, evolutionary changes and corresponding dynamic regimes, *Rev. Geophys.*,
48 684 46, RG4006, doi:10.1029/2008RG000260.
49
50 685 Ben-Zion, Y. and D. J. Andrews, (1998), Properties and Implications of Dynamic Rupture
51 686 Along a Material Interface, *Bull. Seism. Soc. Am.*, 88, 1085-1094.
52
53
54 687 Ben-Zion, Y., T. Rockwell, Z. Shi and S. Xu, (2012). Reversed-polarity secondary
55 688 deformation structures near fault stepovers, *J. of Appl. Mech.*, 79, 031025,
56 689 doi:10.1115/1.4006154.
57
58 690 Ben-Zion, Y. and Sammis, C.G., (2003). Characterization of fault zones, *Pure appl. Geophys.*,
59 691 160, 677–715.
60
61
62
63
64
65

- 692 Ben-Zion, Y. and Z. Shi, (2005). Dynamic rupture on a material interface with spontaneous
1 693 generation of plastic strain in the bulk, *Earth Planet. Sci. Lett.*, 236, 486-496, DOI:
2 694 10.1016/j.epsl.2005.03.025.
3
- 4 695 Boore, D.M. (2014). What do data used to develop ground-motion prediction equations tell us
5 696 about motions near faults?, *Pure and Applied Geophysics*, in press.
6
- 7
8 697 Boness N.L. and M.D. Zoback, (2006). A multiscale study of the mechanisms controlling
9 698 shear velocity anisotropy in the San Andreas Fault Observatory at Depth. *Geophysics*, 71,
10 699 doi:10.1190/1.2231107.
11
- 12 700 Boué P., P. Roux, M. Campillo and B. de Cacqueray (2013) Double beamforming processing
13 701 in a seismic prospecting context. *Geophysics*. Volume : 78 Issue : 3 Pages : V101-V108
14 702 DOI : 10.1190/GEO2012-0364.1
15
- 16
17 703 Campillo, M. and A Paul, 2003, Long-range correlations in the seismic coda, *Science* 299,
18 704 547–549.
19
- 20 705 Campillo, M., Roux, P. & Shapiro, N.M., (2011), Using seismic noise to image and to
21 706 monitor the Solid Earth, in *Encyclopedia of Solid Earth Geophysics*, ed. Gupta, Harsh K.,
22 707 pp. 1230–1235, Springer.
23
- 24
25 708 Campillo, M., S. Singh, N. Shapiro, J. Pacheco, and R. Herrmann (1996), Crustal structure
26 709 south of the Mexican volcanic belt, based on group velocity dispersion, *Geofis. Int.*, 35,
27 710 361–370.
28
- 29 711 Dair, L., and Cooke, M.L., 2009, San Andreas fault geometry through the San Gorgonio Pass,
30 712 California: *The Geological Society of America*, v. 37; no.2, p.119-122.
31
- 32
33 713 Dor, O., Rockwell, T.K. and Ben-Zion, Y., (2006). Geologic observations of damage
34 714 asymmetry in the structure of the San Jacinto, San Andreas and Punchbowl faults in
35 715 southern California: a possible indicator for preferred rupture propagation direction, *Pure
36 716 appl. Geophys.*, 163, 301–349, doi:10.1007/s00024-005-0023-9.
37
- 38 717 Fay, N.P. and Humphreys, E.D., (2005). Fault slip rates, effects of elastic heterogeneity on
39 718 geodetic data, and the strength of the lower crust in the Salton Trough region, southern
40 719 California, *J. geophys. Res.*, 110, B09401, doi:10.1029/2004JB003548.
41
- 42
43 720 Fialko, Y., L. Rivera, and H. Kanamori, (2005). Estimate of differential stress in the upper
44 721 crust from variations in topography and strike along the San Andreas fault, *Geophys. J.
45 722 Int.*, 160, 527-532.
46
- 47 723 Finzi, Y., Hearn, E.H., Lyakhovskiy, V. & Ben-Zion, Y., (2009). Structural properties and
48 724 deformation patterns of evolving strike-slip faults: numerical simulations incorporating
49 725 damage rheology, *Pure appl. Geophys.*, 166, 1537–1573, doi:10.1007/s00024-009-0522-1.
50
- 51
52 726 Froment B. , Campillo M. , Roux P., Gouedard P. , Verdel A., Weaver R.L. (2010),
53 727 Estimation of the effect of nonisotropically distributed energy on the apparent arrival time
54 728 in correlations, *Geophysics*, 75, SA85-SA93, doi:10.1190/1.3483102.
55
- 56 729 Fry, B., F. Deschamps, E. Kissling, L. Stehly, and D. Giardini (2010), Layered azimuthal
57 730 anisotropy of Rayleigh wave phase velocities in the European Alpine lithosphere inferred
58 731 from ambient noise, *Earth Planet. Sci. Lett.*, 297(1), 95–102.
59
60
61
62
63
64
65

- 732 Fuis, S. G., D. Scheirers, E. V. Langenheim, D. M. Koh-
 1 733 Ler, (2012). A New Perspective on
 2 734 the Geometry of the San An-
 3 735 dreas Fault of South California and Relationship to Litho-
 4 spheric Structure, *Bulletin of Seismological Society of America*, Vol. 102, 2012, pp. 236-
 5 1251.
- 6 736 Hauksson, E. (2000), Crustal structure and seismicity distribution adjacent to the Pacific and
 7 737 North America plate boundary in southern California, *J. Geophys. Res.*, 105, 13,875–
 8 738 13,903.
- 9 739 Hauksson, E., W. Yang, and P. M. Shearer, (2012). Waveform Relocated Earthquake Catalog
 11 740 for Southern California (1981 to June 2011); *Bull. Seismol. Soc. Am.*, Vol. 102, No. 5,
 12 741 pp. – doi: 10.1785/0120120010.
- 14 742 Herman, R.B. and Ammon, C.J., (2002). Surface Waves, Receiver Function and Crustal
 16 743 Structure, St. Louis University.
- 17 744 Hillers, G. and Y. Ben-Zion, (2011), Seasonal variations of observed noise amplitudes at 2-18
 19 745 Hz in southern California, *Geophys. J. Int.*, 184, 860–868, doi: 10.1111/j.1365-
 20 746 246X.2010.04886.x.
- 22 747 Hillers, G., Y. Ben-Zion, M. Landès, and M. Campillo (2013), Interaction of microseisms
 23 748 with crustal heterogeneity : A case study from the San Jacinto fault zone area, *Geochem.*
 25 749 *Geophys. Geosyst.*, XX, doi:10.1002/ggge.20140.
- 26 750 Janecke, S.U., Dorsey, R.J., and Belgarde, B., (2010). Age and structure of the San Jacinto
 28 751 and San Felipe fault zones and their lifetime slip rates: In Clifton, H.E., and Ingersoll,
 29 752 R.V., eds., 2010, *Geologic excursions in California and Nevada: tectonics, stratigraphy*
 30 753 *and hydrogeology: Pacific Section, SEPM (Society for Sedimentary Geology) Book 108,*
 32 754 p. 233-271.
- 33 755 Kaneko, Y., and Fialko Y., (2011). Shallow slip deficit due to large strike-slip earthquakes
 35 756 in dynamic rupture simulations with elasto-plastic off-fault response. *Geophysical Journal*
 36 757 *International*. 186:1389-1403.
- 38 758 Kimman W.P. and Trampert J., (2010). Approximations in seismic interferometry and their
 39 759 effects on surface waves, *Geophys. J. Int.*, 182, 461-476.
- 41 760 Kirby, S.M., Janecke, S.U., Dorsey, R.J., Housen, B.A., McDougall, K., Langenheim, V., &
 43 761 Steely, A. (2007). Pleistocene Brawley and Ocotillo formations: evidence for initial
 44 762 strike-slip deformation along the San Felipe and San Jacinto fault zones, *Calif. J. Geol.*
 45 763 115, 43–62.
- 47 764 Kurzon, I., F.L.Vernon, Y. Ben-Zion and G. Atkinson, (2014). Ground Motion Prediction
 49 765 Equations in the San Jacinto Fault Zone – Significant Effects of Rupture Directivity and
 50 766 Fault Zone Amplification, *Pure Appl. Geophys.*, in review.
- 51 767 Landès, M., Hubans, F., Shapiro, N., Paul, A. & Campillo, M., (2010). Origin of deep ocean
 53 768 microseisms by using teleseismic body waves, *J. geophys. Res.*, 115, B05302,
 54 769 doi:10.1029/2009JB006918.
- 56 770 Levshin, A., Yanovskaya, T., Lander, A., Bukchin, B., Barmin, M., Ratnikova, L. & Its, E.,
 58 771 (1989). *Seismic Surface Waves in a Laterally Inhomogeneous Earth*, Kluwer, Dordrecht.
- 59 772 Lewis, M.A., Peng, Z., Ben-Zion, Y. and Vernon, F.L., (2005). Shallow seismic trapping

- 773 structure in the San Jacinto fault zone near Anza, California, *Geophys. J. Int.*, 162, 867–
1 774 881, doi:10.1111/j.1365-246X.2005.02684.x.
2
- 3 775 Lin, F., Moschetti, M. & Ritzwoller, M., (2008). Surface wave tomography of the western
4 776 United States from ambient seismic noise: Rayleigh and Love wave phase velocity maps,
5 777 *Geophys. J. Int.*, 173(1), 281– 298.
6
- 7 778 Lin, F., Ritzwoller, M., Townend, J., Bannister, S. and Savage, M., (2007). Ambient noise
8 779 Rayleigh wave tomography of New Zealand, *Geophys. J. Int.*, 170(2), 649–666.
9
- 10
11 780 Lin, F., Ritzwoller, M. H. and Snieder, R. (2009), Eikonal tomography: surface wave
12 781 tomography by phase front tracking across a regional broad-band seismic array.
13 782 *Geophysical Journal International*, 177: 1091–1110. doi: 10.1111/j.1365-
14 783 246X.2009.04105.x
15
- 16
17 784 Lin, F., M. Ritzwoller, Y. Yang, M. Moschetti, and M. Fouch (2011), Complex and variable
18 785 crustal and uppermost mantle seismic anisotropy in the western United States, *Nat.*
19 786 *Geosci.*, 4(1), 55–61.
20
- 21 787 Lin, G., Thurber, C.H., Zhang, H., Hauksson, E., Shearer, P., Waldhauser, F., Brocher, T.M.
22 788 and Hardebeck, J., (2010). A California statewide three dimensional seismic velocity
23 789 model from both absolute and differential times, *Bull. seism. Soc. Am.*, 100, 225–240.
24
- 25
26 790 Lin, G., P. M. Shearer, E. Hauksson, and C. H. Thurber (2007), A three-dimensional crustal
27 791 seismic velocity model for southern California from a composite event method, *J.*
28 792 *Geophys. Res.*, 112, B11306, doi:10.1029/2007JB004977.
29
- 30 793 Lindsey, E. O., and Y. Fialko (2013), Geodetic slip rates in the southern San Andreas Fault
31 794 system: Effects of elastic heterogeneity and fault geometry, *J. Geophys. Res. Solid Earth*,
32 795 118, 689–697, doi:10.1029/2012JB009358
33
34
- 35 796 Liu, Y., T. L. Teng and Y. Ben-Zion, (2005). Near-surface seismic anisotropy, attenuation
36 797 and dispersion in the aftershock region of the 1999 Chi-Chi, earthquake, *Geophys. J. Int.*,
37 798 160, 695-706.
38
- 39 799 Magistrale, H., and C. Sanders (1996), Evidence from precise earthquake hypocenters for
40 800 segmentation of the San Andreas Fault in San Geronio Pass, *J. Geophys. Res.*, 101(B2),
41 801 3031–3044, doi:10.1029/95JB03447.
42
43
- 44 802 Marilyani, G.I., Rockwell, T.K., Onderdonk, N.H., & McGill, S.F (2013). Straightening of the
45 803 Northern San Jacinto Fault, California as Seen in the Fault-structure Evolution of the San
46 804 Jacinto Valley Stepover, *Bull. Seismol. Soc. Am.* 103(3).
47
- 48 805 Mordret, A., N. M. Shapiro, S. Singh, P. Roux, J.P. Montagner and O. I. Barkved, (2013).
49 806 Azimuthal anisotropy at Valhall: the Helmholtz equation approach, *Geophysical Research*
50 807 *Letter*, doi: 10.1002/grl.50447.
51
52
- 53 808 Morton, N., Girty, G.H. and Rockwell, T.K., (2012). Fault zone architecture of the San
54 809 Jacinto fault zone in Horse Canyon, southern California: a model for focused post-seismic
55 810 fluid flow and heat transfer in the shallow crust, *Earth planet. Sci. Lett.*, 330, 71–83,
56 811 doi:10.1016/j.espl.2012.02.0
57
- 58
59 812 Morton, D.M., and Matti, J.C., 1993, Extension and contraction within an evolving divergent
60 813 strike-slip fault complex: The San Andreas and San Jacinto fault zones at their
61
62
63
64
65

- 814 convergence in southern California, in Powell, R.E., Weldon, R.J.,II, and Matti, J.C., eds.,
1 815 The San Andreas fault system: Displacement, palinspastic reconstruction, and geologic
2 816 evolution: Geological Society of America, Memoir 178, Chapter 5, p. 217-230.
3
- 4 817 Moschetti, M., Ritzwoller, M. & Shapiro, N., (2007). Surface wave tomogra- phy of the
5 818 western United States from ambient seismic noise: Rayleigh wave group velocity maps,
6 819 *Geochem. Geophys. Geosyst.*, 8, Q08010, doi:10.1029/2007GC001655.
8
- 9 820 Moschetti, M.P., Ritzwoller, M.H., Lin, F.C., Yang, Y., (2010). Crustal shear velocity
10 821 structure of the western US inferred from ambient noise and earthquake data. *J. Geophys.*
11 822 *Res.* 115, B10306 doi:10.1029/ 2010JB007448.
12
- 13 823 Onderdonk, N.W. (1998). The tectonic structure of the Hot Springs fault zone, Riverside
14 824 County, California [Ph.D. Thesis]: California State University, Long Beach, California.
16
- 17 825 Peng, Z., and Y. Ben-Zion (2004), Systematic analysis of crustal anisotropy along the
18 826 Karadere-Du`zce branch of the north Anatolian fault, *Geophys. J. Int.*, 159, 253– 274,
19 827 doi:10.1111/j.1365-246X.2004.02379.x.
20
- 21 828 Poli P., H. A. Pedersen, M. Campillo, and the POLENET/LAPNET Working Group (2013),
22 829 Noise directivity and group velocity tomography in a region with small velocity contrasts
23 830 : the northern Baltic Shield. *Geophysical Journal International* 192, 413–424.
25
- 26 831 Ritzwoller, M.H., F.C. Lin, and W. Shen (2011), Ambient noise tomography with a large
27 832 continental seismic array, *Compte Rendus Geoscience*, 13 pages,
28 833 doi:10.1016/j.crte.2011.03.007.
29
- 30 834 Rockwell, T., Loughman, C. and Merifield, P., (1990). Late Quaternary rate of slip along the
31 835 San Jacinto fault zone near Anza, Southern California, *J. geophys. Res. B*, 95(6), 8593–
32 836 8605.
34
- 35 837 Rockwell, T.K., Seitz, G.G., Dawson, T.E. and Young, J., (2006). The long record of San
36 838 Jacinto Fault paleoearthquakes at Hog Lake; implications for regional patterns of strain
37 839 release in the southern San Andreas Fault system, *Seismol. Res. Lett.*, 77, 270–296.
38
- 39 840 Rockwell, T. K., T. E. Dawson, J. Young and Gordon Seitz (2014), A 21 event, 4,000-year
40 841 history of surface ruptures in the Anza Seismic Gap, San Jacinto Fault: Implications for
41 842 long-term earthquake production on a major plate boundary fault, *Pure Appl. Geophys.*, in
42 843 review.
44
- 45 844 Roux, P. and Y. Ben-Zion, (2014). Monitoring fault zone environments with correlations of
46 845 earthquake waveforms, *Geophys. J. Int.*, 196, doi: 10.1093/gji/ggt441.
47
- 48 846 Roux, P., Wathelet, M. and Roueff, A., (2011). The San Andreas Fault revisited through
49 847 seismic-noise and surface-wave tomography, *Geophys. Res. Lett.*, 38, L13319,
50 848 doi:10.1029/2011GL047811.
52
- 53 849 Sabra, K. G., P. Gerstoft, P. Roux, W. A. Kuperman, and M. C. Fehler (2005a), Extracting
54 850 time-domain Greens function estimates from ambient seismic noise, *Geophys. Res. Lett.*,
55 851 32, L03310, doi:10.1029/2004GL021862.
56
- 57 852 Sabra, K. G., P. Gerstoft, P. Roux, W. A. Kuperman, and M. C. Fehler (2005b), Surface wave
58 853 tomography from microseisms in Southern California, *Geophys. Res. Lett.*, 32, L14311,
59 854 doi:10.1029/2005GL023155.
60 854

- 855 Salisbury, J.B., Rockwell, T.K., Middleton, T.J. and Hudnut, K.W., (2012). LiDAR and field
1 856 observations of slip distribution for the most recent surface ruptures along the central San
2 857 Jacinto Fault, *Bull. seism. Soc. Am.*, 102, 598–619, doi:10.1785/0120110068.
3
- 4 858 Schulte-Pelkum, V., P. S. Earle, and F. L. Vernon (2004), Strong directivity of ocean-
5 859 generated seismic noise, *Geochem. Geophys. Geosyst.*, 5, Q03004,
6 860 doi:10.1029/2003GC000520.
7 861
- 8
9 861 Seeber, L., and J. G. Armbruster (1995), The San Andreas Fault system through the
10 862 Transverse Ranges as illuminated by earthquakes, *J. Geophys. Res.*, 100(B5), 8285–8310,
11 863 doi:10.1029/94JB02939.
12
- 13 864 Shapiro, N. and Campillo, M., (2004). Emergence of broadband Rayleigh waves from
14 865 correlations of the ambient seismic noise, *Geophys. Res. Lett.*, 31(7),
15 866 doi:10.1029/2004GL019491.
16 867
- 17
18 867 Shapiro, N.M., Campillo, M., Stehly, L. and Ritzwoller, M.H., (2005). High resolution
19 868 surface-wave tomography from ambient seismic noise, *Science*, 29, 1615–1617.
20
- 21 869 Sharp, R.V., (1967). San Jacinto fault zone in the Peninsular Ranges of south-
22 870 ern California, *Geol. Soc. Am. Bull.*, 78, 705–730.
23
- 24
25 871 Shi, Z. and Y. Ben-Zion, (2006). Dynamic rupture on a bimaterial interface governed by slip-
26 872 weakening friction, *Geophys. J. Int.*, 165, 469-484, doi: 10.1111/j.1365-
27 873 246X.2006.02853.x.
28
- 29 874 Smith, M., and F. Dahlen (1973), The azimuthal dependence of Love and Rayleigh wave
30 875 propagation in a slightly anisotropic medium, *J. Geophys. Res.*, 78(17), 3321–3333.
31
- 32 876 Stehly, L, M. Campillo and N. Shapiro (2006), A Study of the seismic noise from its long-
33 877 range correlation properties, *Journal of Geophysical research*, Vol 111, B10306.
34
- 35
36 878 Stehly, L., Fry, B., Campillo, M., Shapiro, N. M., Guilbert, J., Boschi, L. and Giardini, D.
37 879 (2009), Tomography of the Alpine region from observations of seismic ambient noise.
38 880 *Geophysical Journal International*, 178: 338–350. doi: 10.1111/j.1365-246X.2009.04132.x
39
- 40 881 Tape, C., Q. Liu, A. Maggi, and Tromp, J., (2010). Seismic tomography of the southern
41 882 California crust based on spectral-element and adjoint methods, *Geophys. J. Int.*, 180,
42 883 433–462.
43 884
- 44
45 884 Wechsler, N., Rockwell, T.K. and Ben-Zion, Y., (2009). Analysis of rock damage asymmetry
46 885 from geomorphic signals along the trifurcation area of the San-Jacinto Fault,
47 886 *Geomorphology*, 113, 82–96.
48 887
- 49 888 Weaver, R.L., B. Froment and M. Campillo, (2009), On the correlation of non-isotropically
50 889 distributed ballistic scalar diffuse waves: *Journal of the Acoustical Society of America*,
51 889 126 (4), 1817-1826, doi:10.1121/1.3203359.
52 890
- 53 891
54 892 Yang, H. and Zhu, L., (2010). Shallow low-velocity zone of the San Jacinto fault from local
55 893 earthquake waveform modelling, *Geophys. J. Int.*, 183, 421–432.
56 894
- 57 894
58 895 Yang, Y., Ritzwoller, M., Levshin, A. & Shapiro, N., (2007). Ambient noise Rayleigh wave
59 896 tomography across Europe, *Geophys. J. Int.*, 168, 259– 274.
60
61
62
63
64
65

897

1 898 Yang, Z., A. Sheehan, and P. Shearer (2011), Stress induced upper crustal anisotropy in
2 899 southern California, *J. Geophys. Res.*, 116, B02302, doi:10.1029/2010JB007655.

3 900

4 901 Yule, D., and K. Sieh (2003), Complexities of the San Andreas fault near San Geronio Pass:
5 902 Implications for large earthquakes, *J. Geophys. Res.*, 108, 2548,

6 903

7 904

8 904

9 905

10 906

11 907

12 908

13 909

14 910

15 911

16 911

17 911

18

19 912

20 912

21

22 913

23 914

24 915

25 916

26 917

27 918

28 919

29 920

30 920

31 921

32 922

33 923

34 924

35 925

36 926

37 927

38 928

39 929

40 930

41 931

42 932

43 932

44 932

45 932

46 932

47 932

48 932

49 932

50 932

51 932

52 932

53 932

54 932

55 932

56 932

CAPTIONS:

Figure 1: Map of the southern California plate boundary region with 158 seismic stations used in this study (red triangles). The fine black lines indicate the fault traces with the San Andreas Fault (SAF), the San Jacinto Fault Zone (SJFZ) and the Elsinore Fault (EF). The blue dots show the seismicity (Hauksson et al., 2012). The blue triangles are the examples stations (paths in purple) discussed in Figure 2. Cross-sections of velocity along profiles 1-7 (black lines) are shown in Figures 13 and 14. The background color indicate the topography with green and brown being low and high elevations respectively. The insert indicates the location of the main map in California.

Figure 2: Examples of paths: PLM-PSD perpendicular to the coast and the SJFZ (Left figures) and PER-BOR along these structures (Right figures). The stations locations and the discussed paths are indicated on Figure 1. Dailly ZZ correlations are plotted as correlograms in (A) and (D). (B-E) Stacked cross-correlation for the entire year 2012 between PLM and PSD (B) and PER and BOR (E). The components are indicated on the figure. Rayleigh waves are observed on the ZZ, ZR, RZ and RR components and Loves waves are obtained on the TT component. (C-F) Period-group velocity diagrams resulting from the combination of the ZZ, ZR, RZ and RR components with a logarithm stacking method describe in section 4.1. The black lines indicate the measured Rayleigh waves dispersion curves and the range on which they are used in the inversion.

Figure 3: Correlation time in seconds as a function of inter-stations distances for the 9 components of the correlation tensor (the components are indicated above the panels). The

933 correlations are stacked for each 0.5km distance bin. Clear Rayleigh waves are reconstruct on
934 the RR, RZ, ZR and ZZ components. Love wave is reconstruct on the TT component. Note
935 the overall good symmetry of the correlations functions. The colors indicate the amplitudes
936 (positive in white and negative in black) with the same scale on all panels.

937 **Figure 4:** Histograms of dispersions measurements at 7 seconds for Rayleigh (A) and Love
938 waves (B) for all the pair of stations. The green lines indicate the mean values and the red
939 lines 2 standard deviations. Only the measurements within these 2 std will be conserved for
940 the inversions.

941 **Figure 5:** Azimuthal distributions of the selected dispersions at 7s (see figure 4) for Rayleigh
942 (A) and Love (B) waves respectively. The small black dots are the group velocity
943 measurements. The large red dots are the group velocity averaged over 10° bins with error
944 bars indicating the standard deviations. The thick blue curves are the best fits for the 2θ and
945 4θ azimuthal variations obtained with equation (2). (C-D) Values of the fitted parameters as a
946 function of period. (C) Values of parameters A and B of equation (2) for Love (dashed) and
947 Rayleigh (continuous). (D) Best fitting angles for Love (dashed) and Rayleigh (continuous).

948 **Figure 6:** Azimuthal 2θ anisotropy maps with fast directions and amplitudes of 7s Rayleigh
949 (A) and Love (B) waves.

950 **Figure 7:** Rayleigh group velocity maps at 3s (A), 5s (B), 7s (C) and 9s (D). The colorbar
951 show the Rayleigh waves group velocities in km/s.

952 **Figure 8:** Love group velocity maps at 3s (A), 5s (B), 7s (C) and 9s (D). The colorbar show
953 the Rayleigh waves group velocities in km/s.

954 **Figure 9:** Number of paths per cell at 7s of period for Rayleigh (A) and Love waves (B). The
955 path coverage is high for all the regions between the Elsinore Fault and the San Andreas
956 Fault. (C) and (D) show the value of the resolution length at 7s for Rayleigh (C) and Love (D)
957 waves. The resolution is good (small correlation length) for most of the region of interest with
958 a mean correlation length of about 3 to 4km. The resolution is lower for Love waves due to
959 the fewer number of paths (4182 paths for Rayleigh waves versus 3014 paths for Love waves
960 at 7s, see table 1).

961 **Figure 10:** (A) Average shear wave velocity model of the area obtained from Rayleigh (blue
962 curve) and Love (red curve) waves group velocity maps. The dashed black line shows the

963 average Allam & Ben-Zion (2012) model use here as the initial model for the inversions. (B-
964 C) Average dispersion curves (blue line) and theoretical curves associated with the models of
965 (A) for Rayleigh (B) and Love waves (C). (D) Misfit as a function of period between the two
966 curves of (B) (blue trace) and (C) (red trace). (E-F) Resolution matrix of the average
967 dispersion curves inversions for Rayleigh (E) and Love (F). (G-H) Histograms of misfits for
968 the local shear wave inversions using Rayleigh (G) and Love (H) waves dispersion curves.
969 The histograms present the misfit between the observed and synthetic dispersion curves for
970 each cell when all the periods are considered.

Figure 11: Map views of V_s at various depths (indicated above the panels) obtained from Rayleigh waves dispersions. The velocity scale is in m/s and is variable for increased visual resolution. Clear velocity contrasts are observed across the SJFZ, the southern SAF and the southern Elsinore fault. The SJFZ and the SAF are marked with low velocity zones in the top 5 km associated to damage zones and basins. The complex region associated with the merging SJFZ and SAF, presents strong velocity reduction in the top 5 km.

Figure 12: Map views of V_s at various depths obtained from Love waves dispersions. The velocity scale is in m/s and is variable for increased visual resolution. As shown in Figure 10f the resolution at 7km is poor. The results show clear velocity contrast and low velocity zones associated with the main faults that are consistent with those obtained with Rayleigh waves (see Figure 11).

Figure 13: Fault normal cross-sections of the shear wave velocity extracted from Rayleigh wave model. The zeros indicate the position of the SJFZ on each profile. The locations of the cross sections are plotted in Figure 1. The velocity scale is in km/s and is variable for increased visual resolution. We observed lateral and depth variations of the velocity contrast and low velocity zones associated with the SJFZ. A strong velocity reduction that extend up to 4km depth is associated to the complex region where the SJFZ and the SAF merges (profiles 3 and 4).

Figure 14: Fault normal cross-sections of the shear wave velocity extracted from Love wave model. The zeros indicate the position of the SJFZ on each profile. The velocity scale is in km/s and is variable for increased visual resolution. The observed velocity contrast and damage zones are in good agreement with the results obtained from Rayleigh waves (see Figure 13).

994 **Figure 15:** 3D Vs map view obtained from the inversion of Rayleigh waves group velocity.

995 The colorbar indicates the shear wave velocity in m/s. Clear velocity contrasts and low

996 velocity zones flower structure are observed.

997

998 **Table 1:**

Period (s)	3	4	5	6	7	8	9	10	11	12
Love	2410	3068	3176	3122	3014	2858	2577	2322	1896	1457
Rayleigh	2881	4315	4542	4442	4182	3678	2781	2045	1379	810

999

1000 **Table 1:** Number of selected paths for each period.

1001 **Figure S1:** (A) Raw data for January 3, 2009, with an earthquake. (B) Same data after

1002 clipping at 4 std. (C) Same data after pre-processing using the sub-segment method (Poli et al,
1003 2012).

1004 **Figure S2:** (A) Cross correlation between PLM and KNW stations obtained for January 3,
1005 2009 after clipping at 4 std (red trace). The blue trace corresponds to the same pair but for a
1006 reference day (January 8, 2009) chosen for it's good and clean noise. (B) Same as (A) but
1007 with the Poli et al, (2012) pre-processing method applies (see the data on Figure S1C).

1008

1009

1010

1011

Figure 1
[Click here to download high resolution image](#)

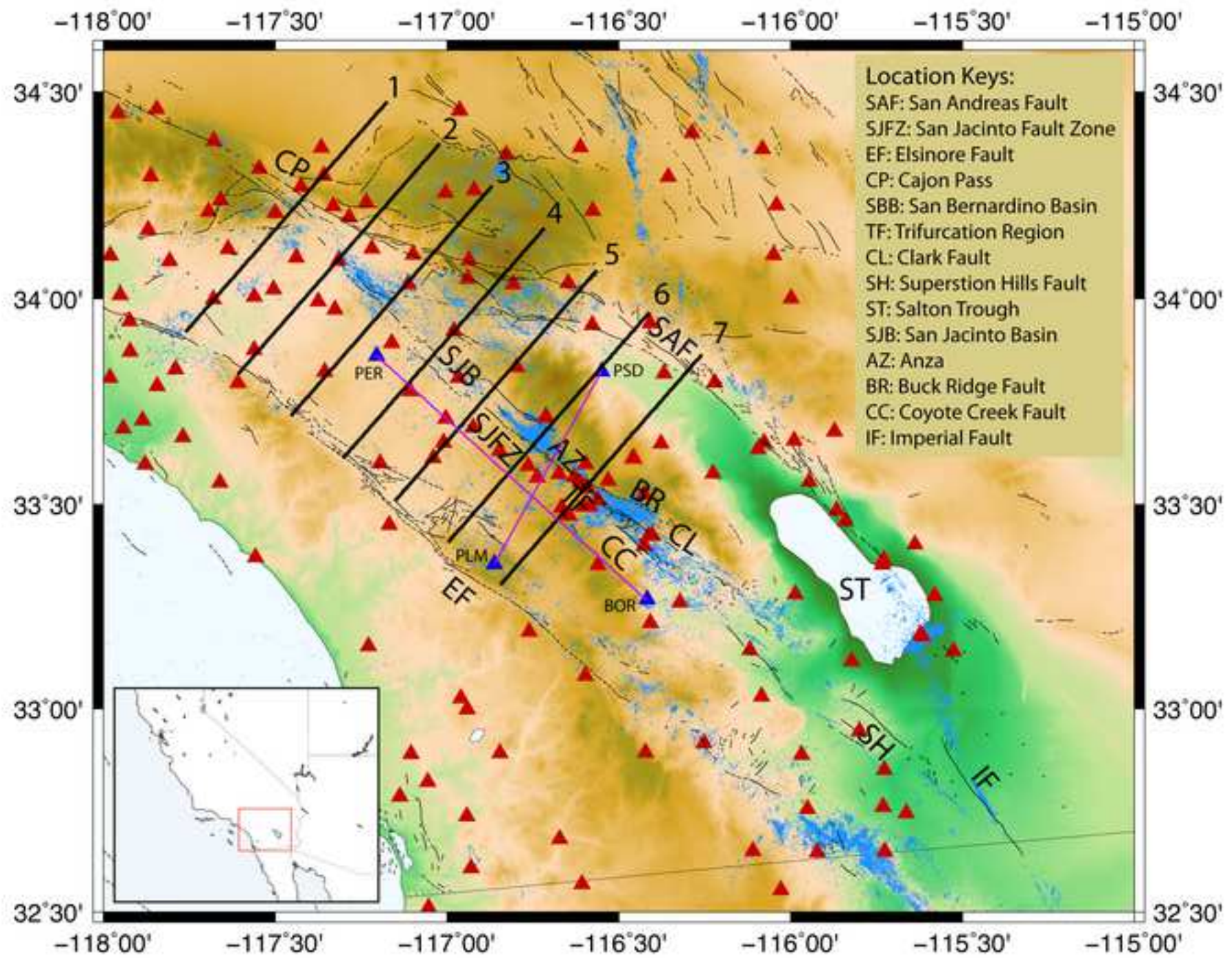


Figure 2
[Click here to download high resolution image](#)

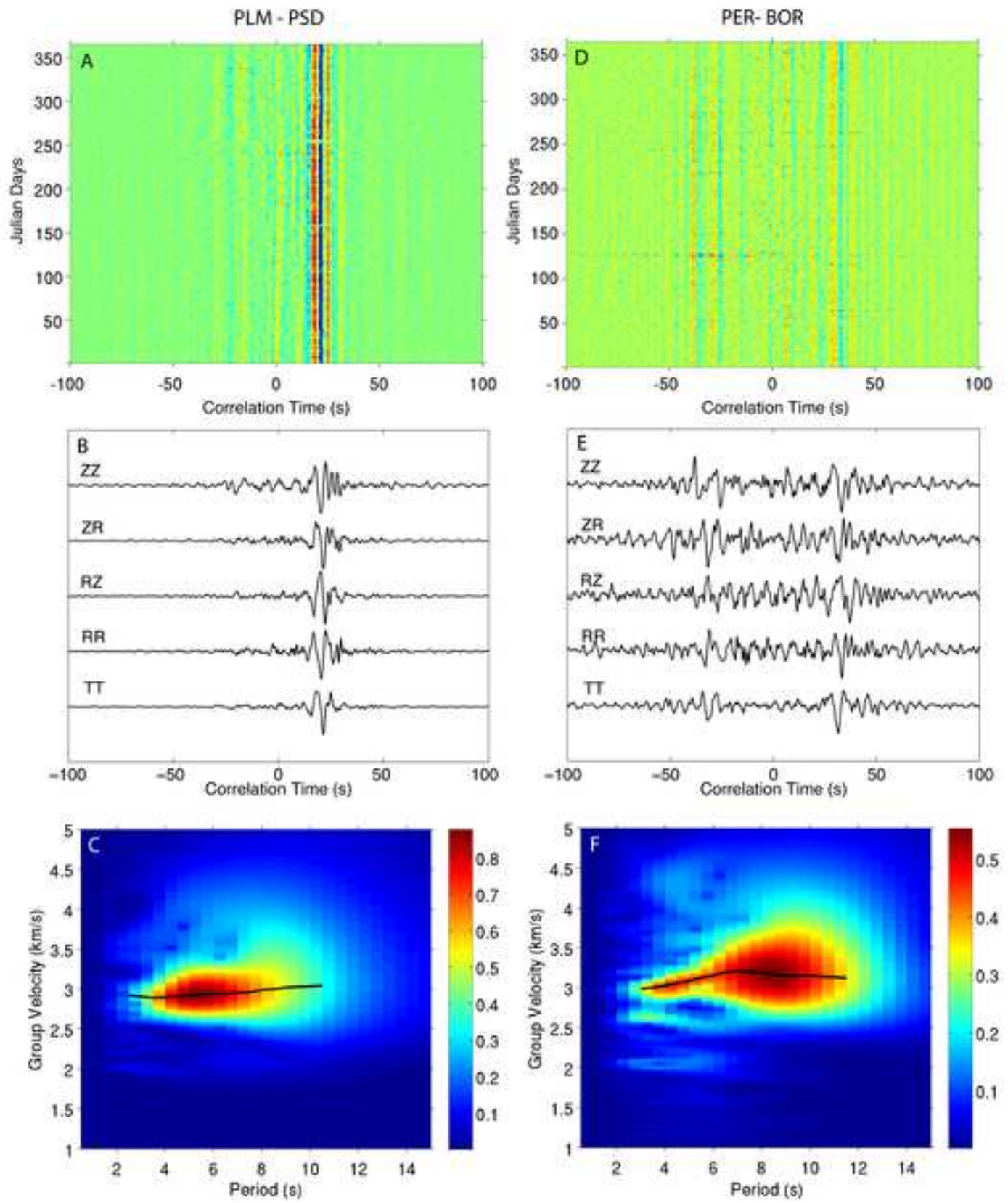


Figure 3
[Click here to download high resolution image](#)

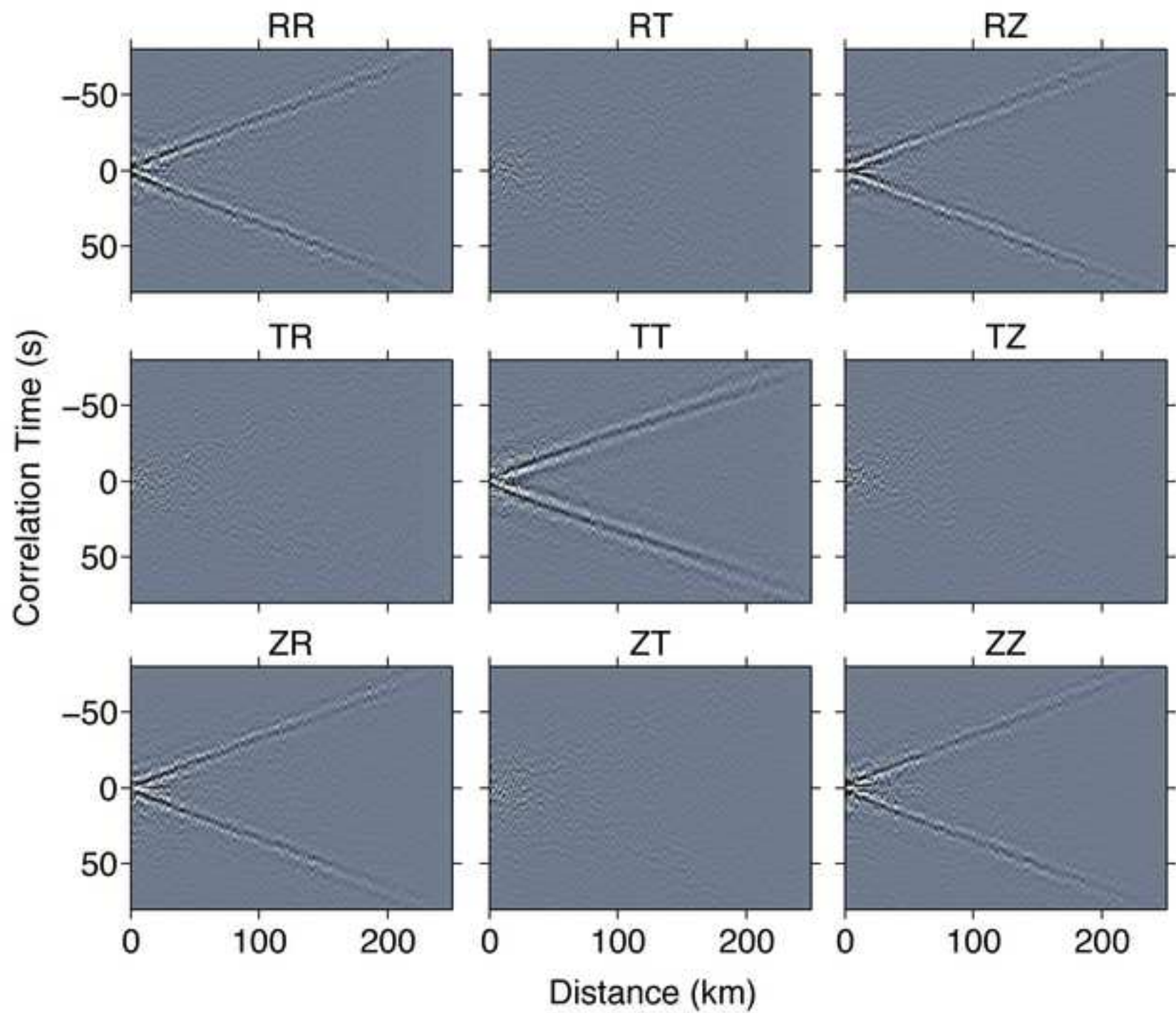


Figure 4
[Click here to download high resolution image](#)

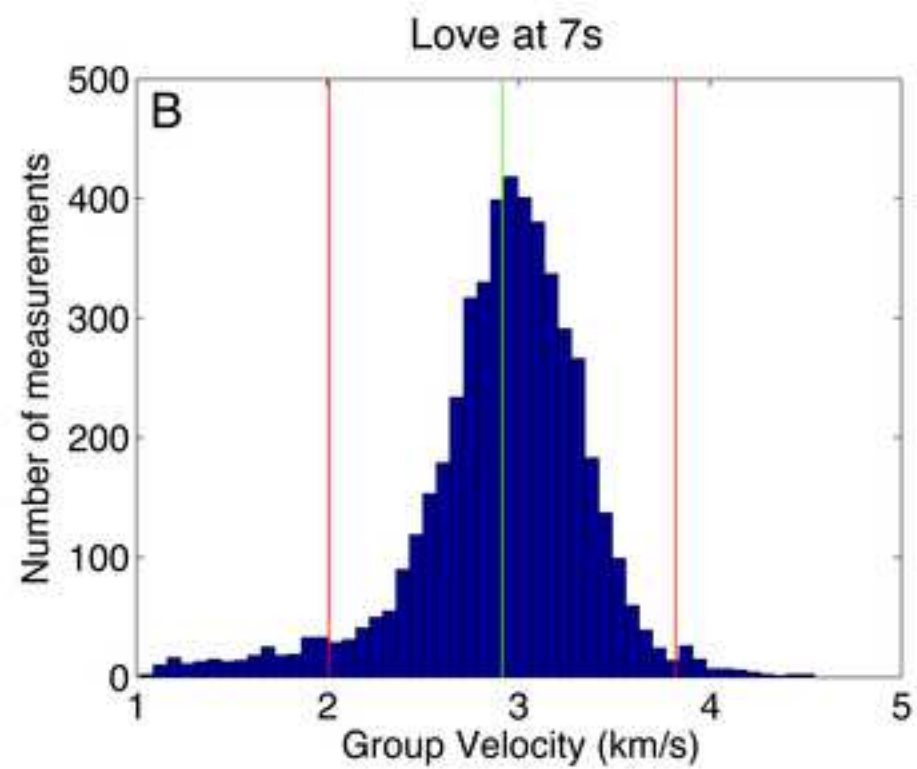
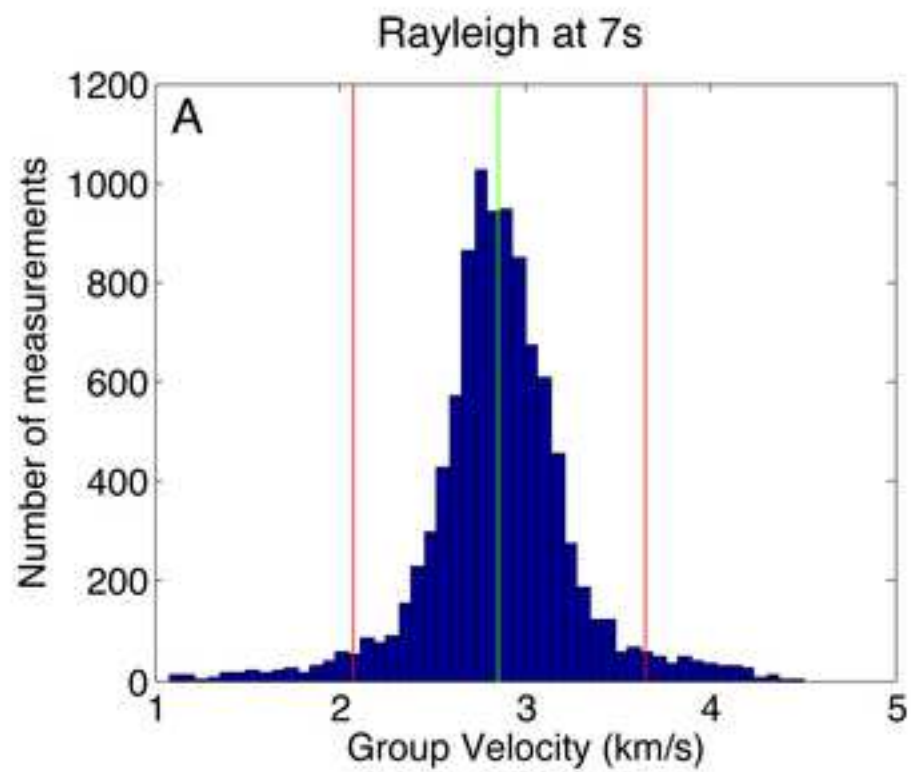


Figure 5
[Click here to download high resolution image](#)

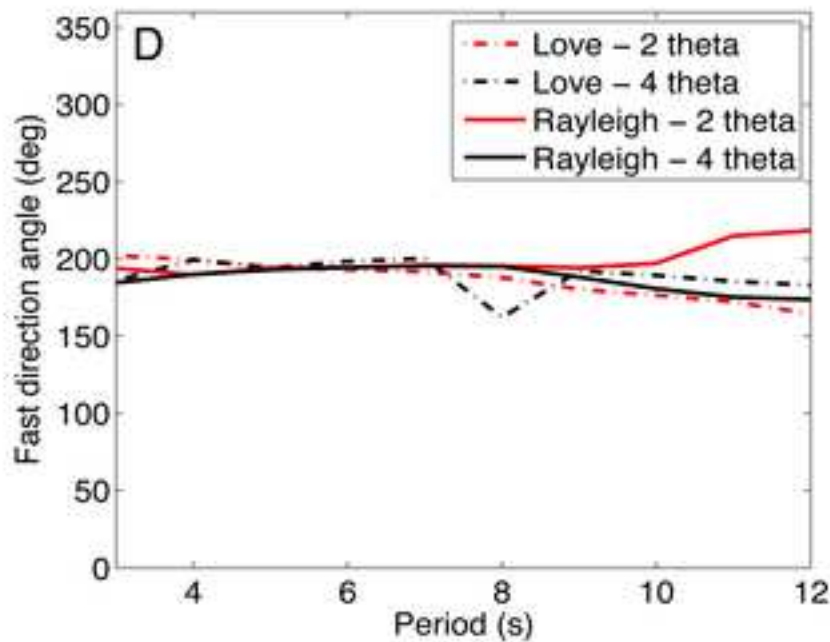
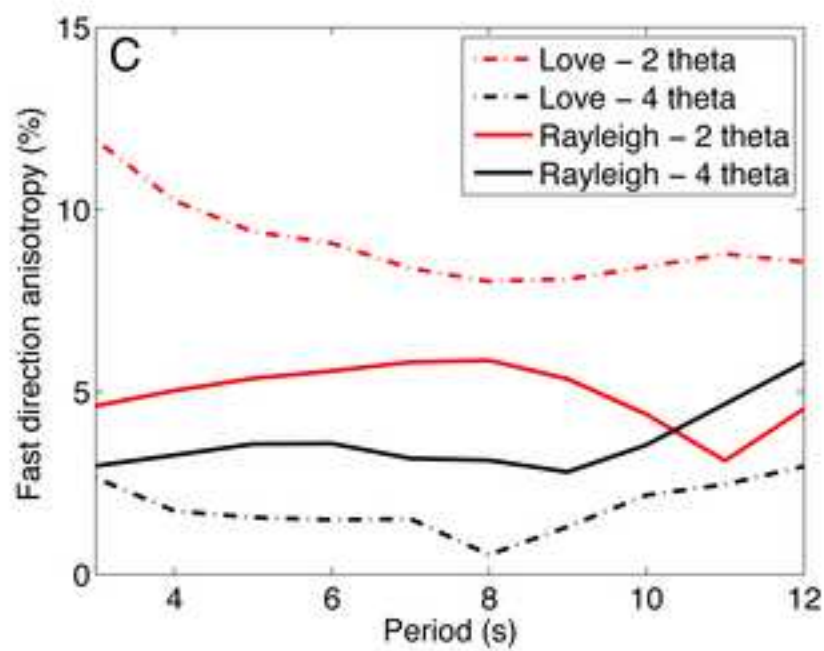
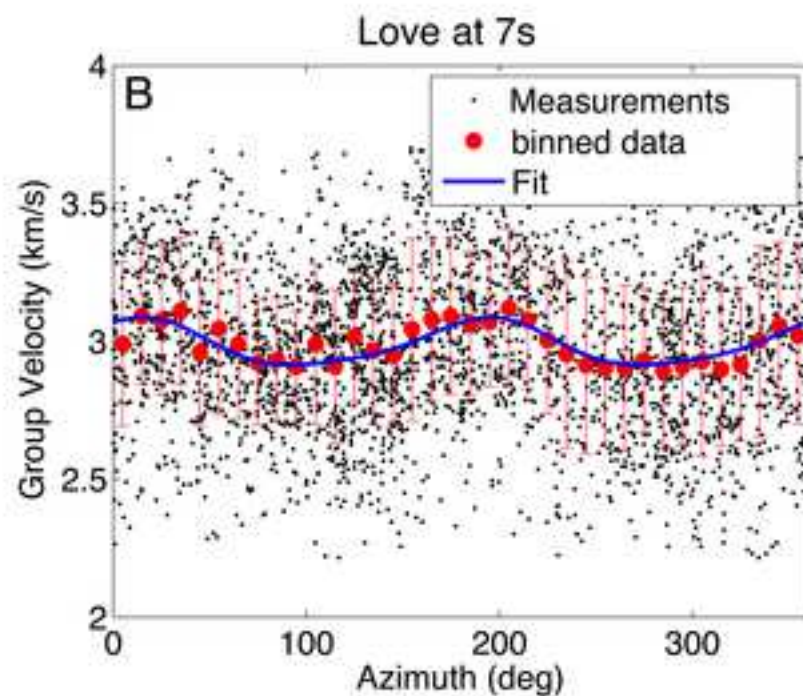
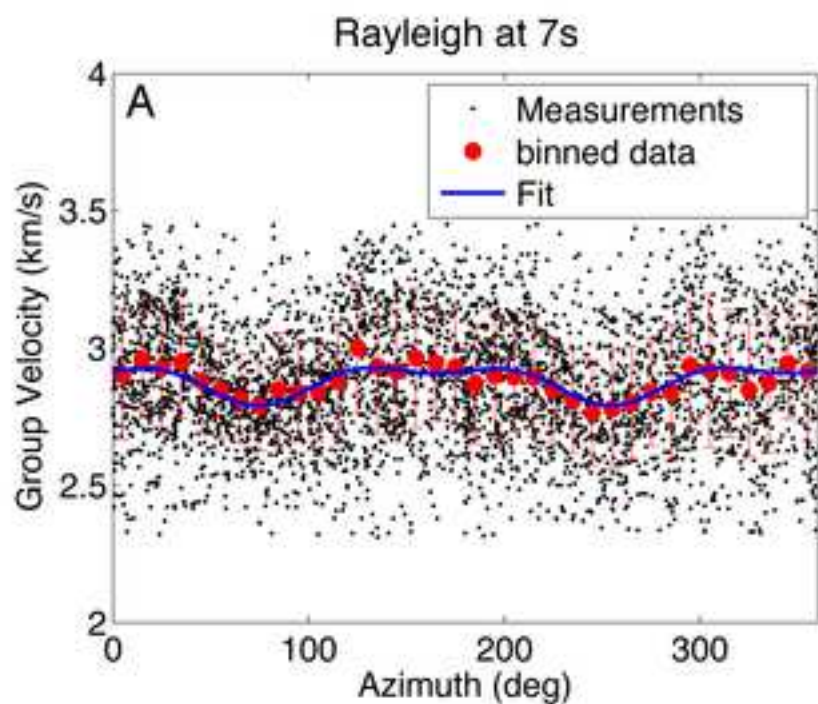


Figure 6
[Click here to download high resolution image](#)

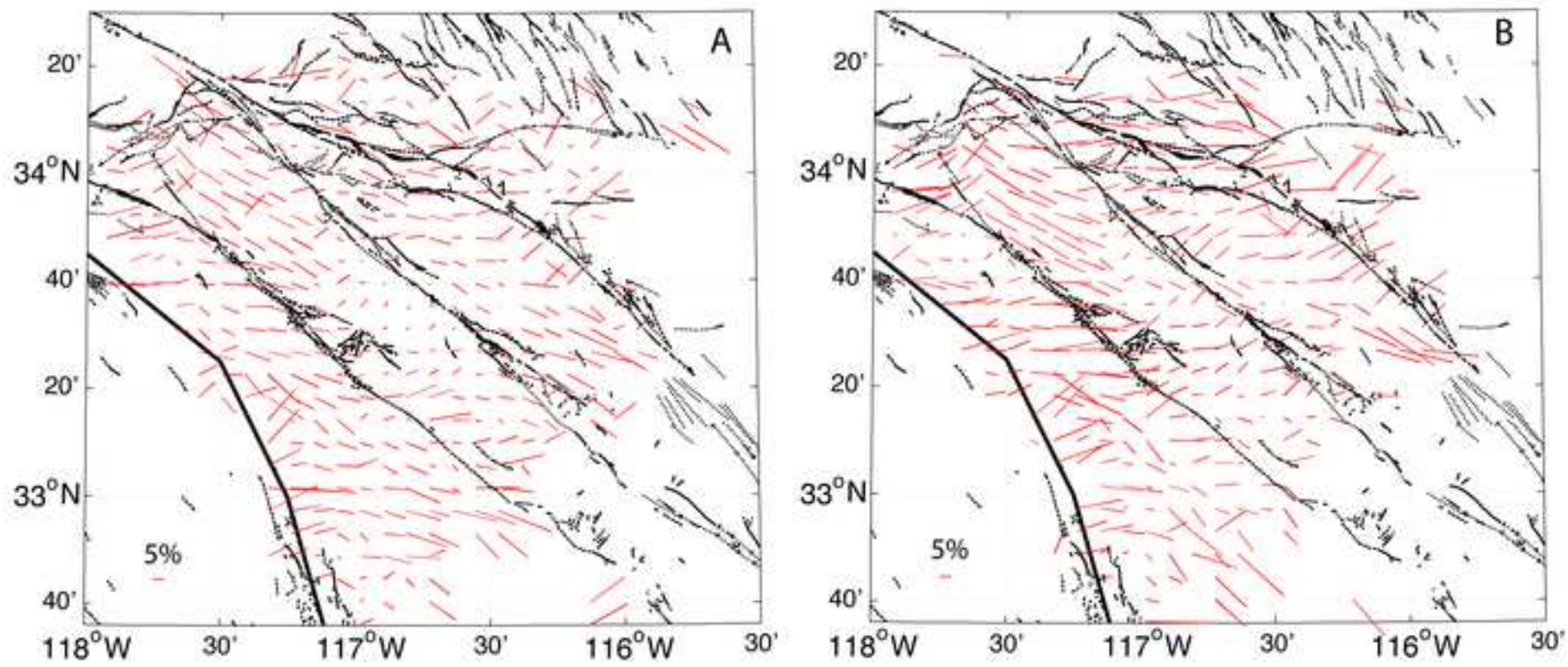


Figure 7
[Click here to download high resolution image](#)

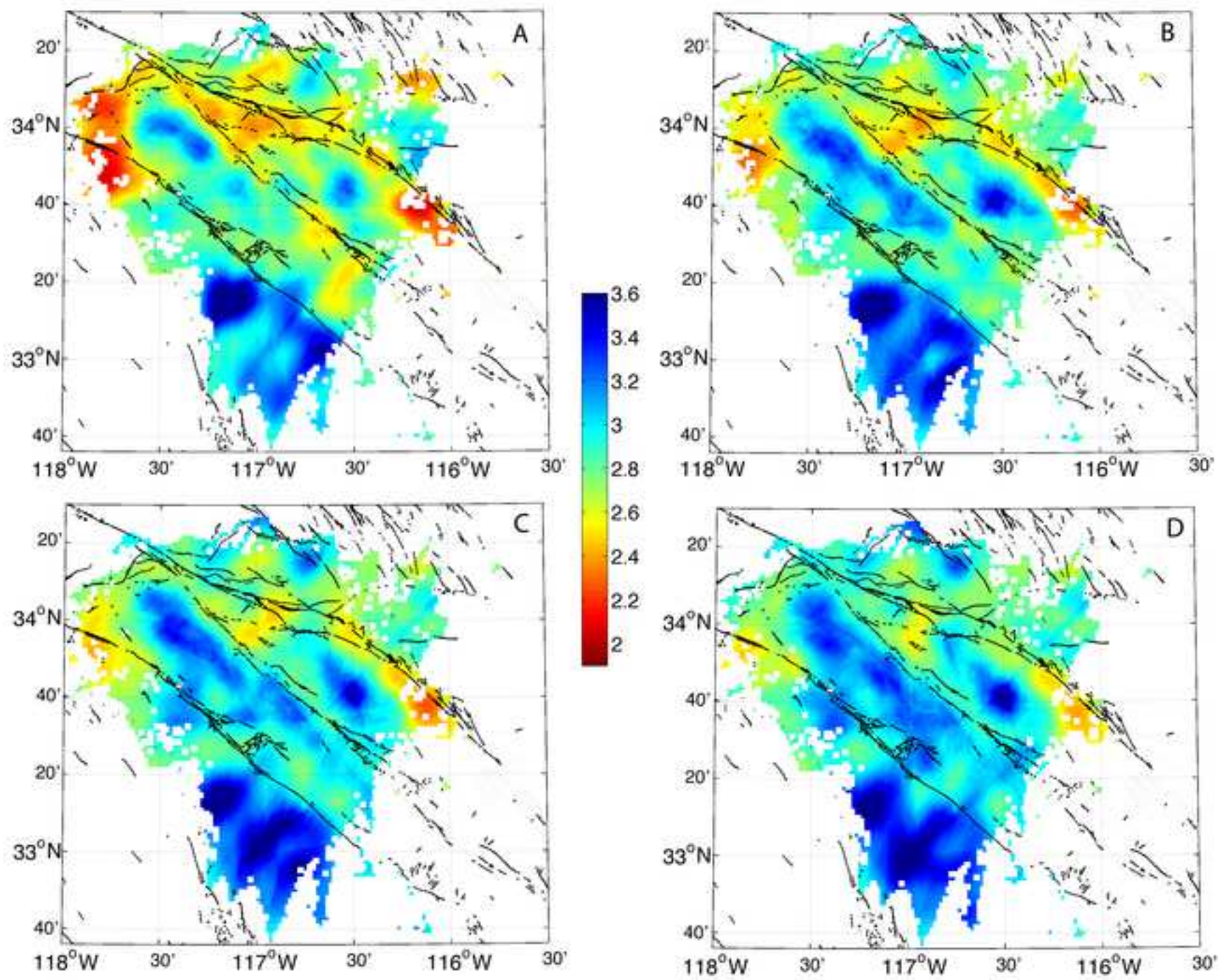


Figure 8
[Click here to download high resolution image](#)

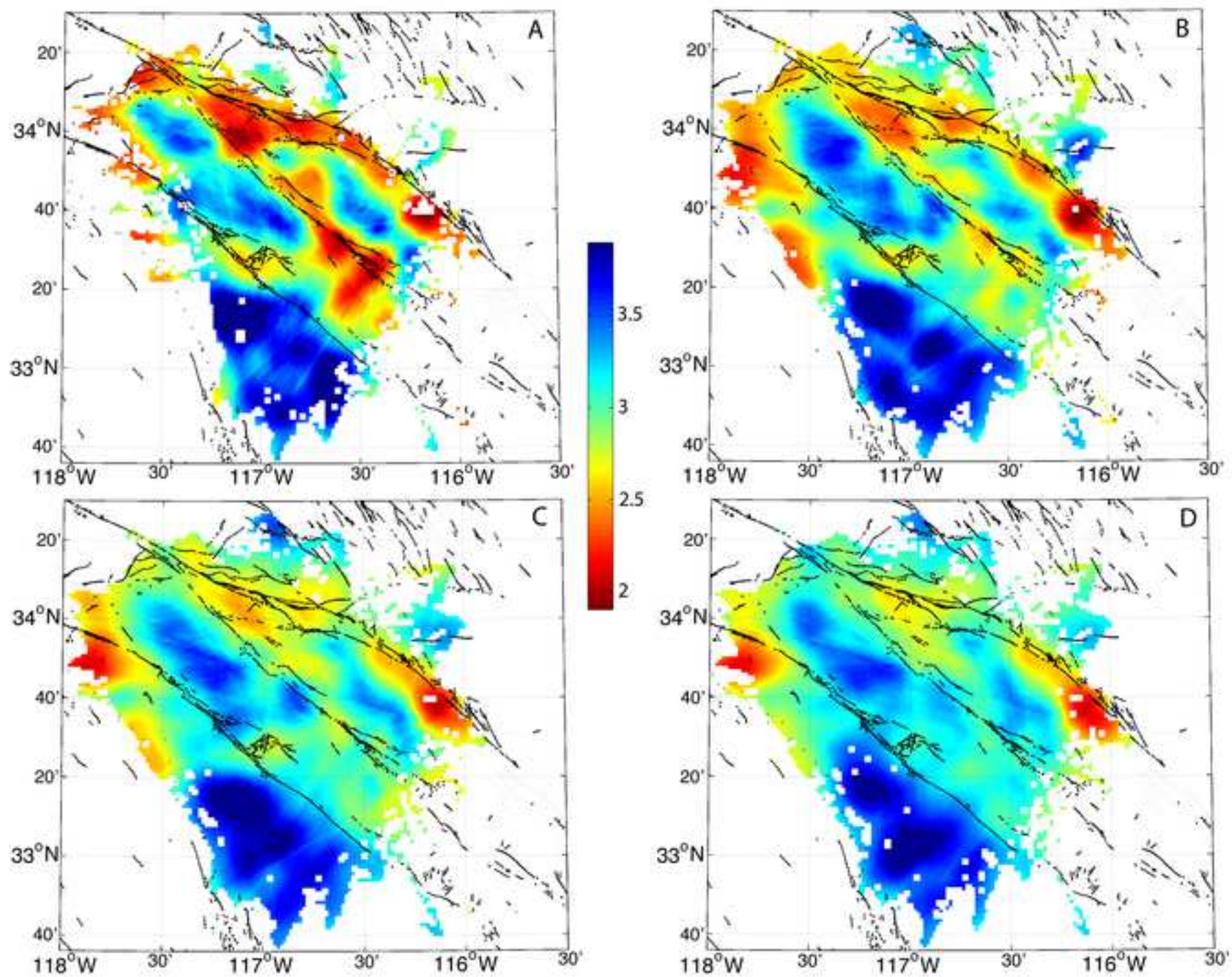


Figure 9
[Click here to download high resolution image](#)

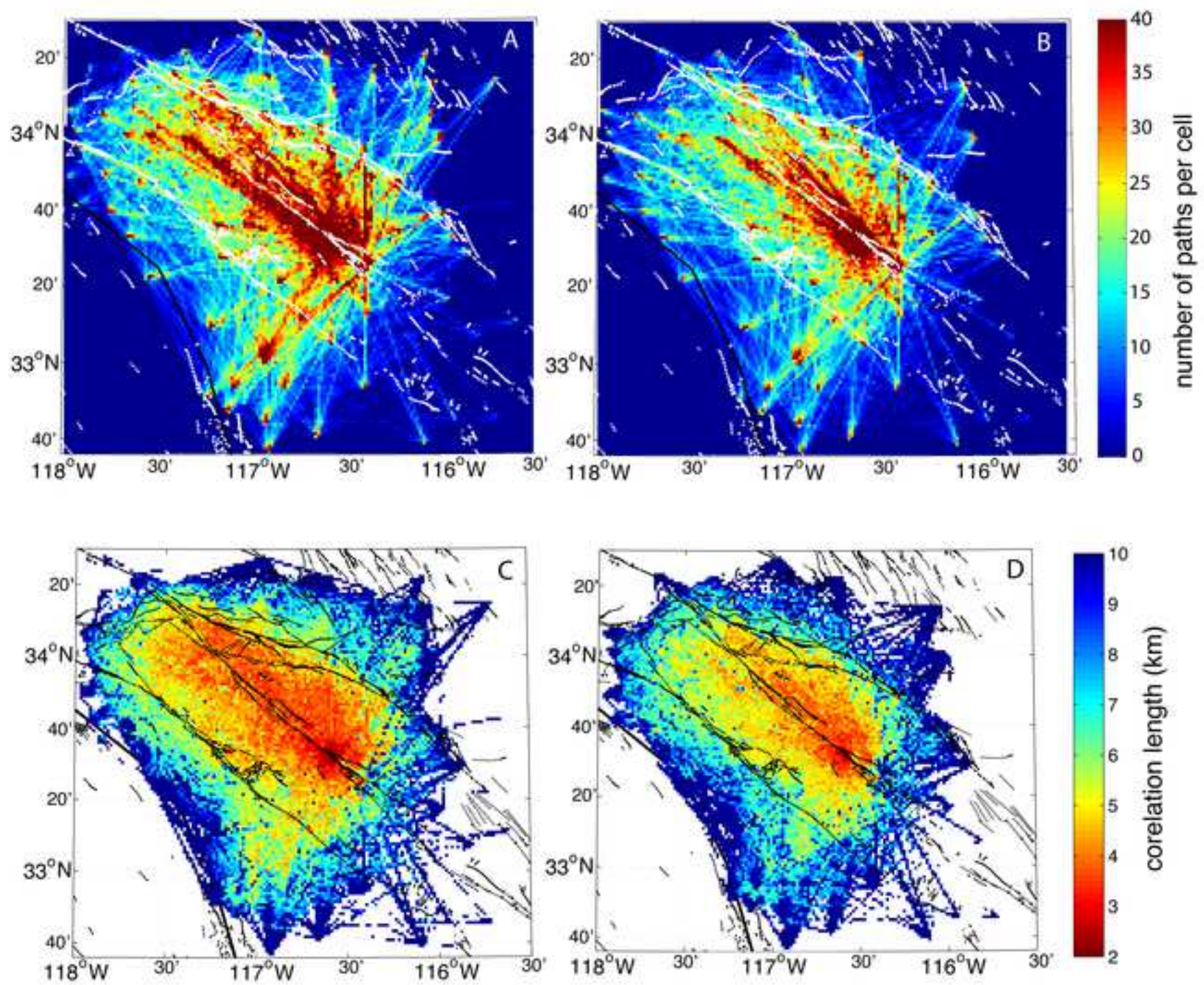


Figure 10
[Click here to download high resolution image](#)

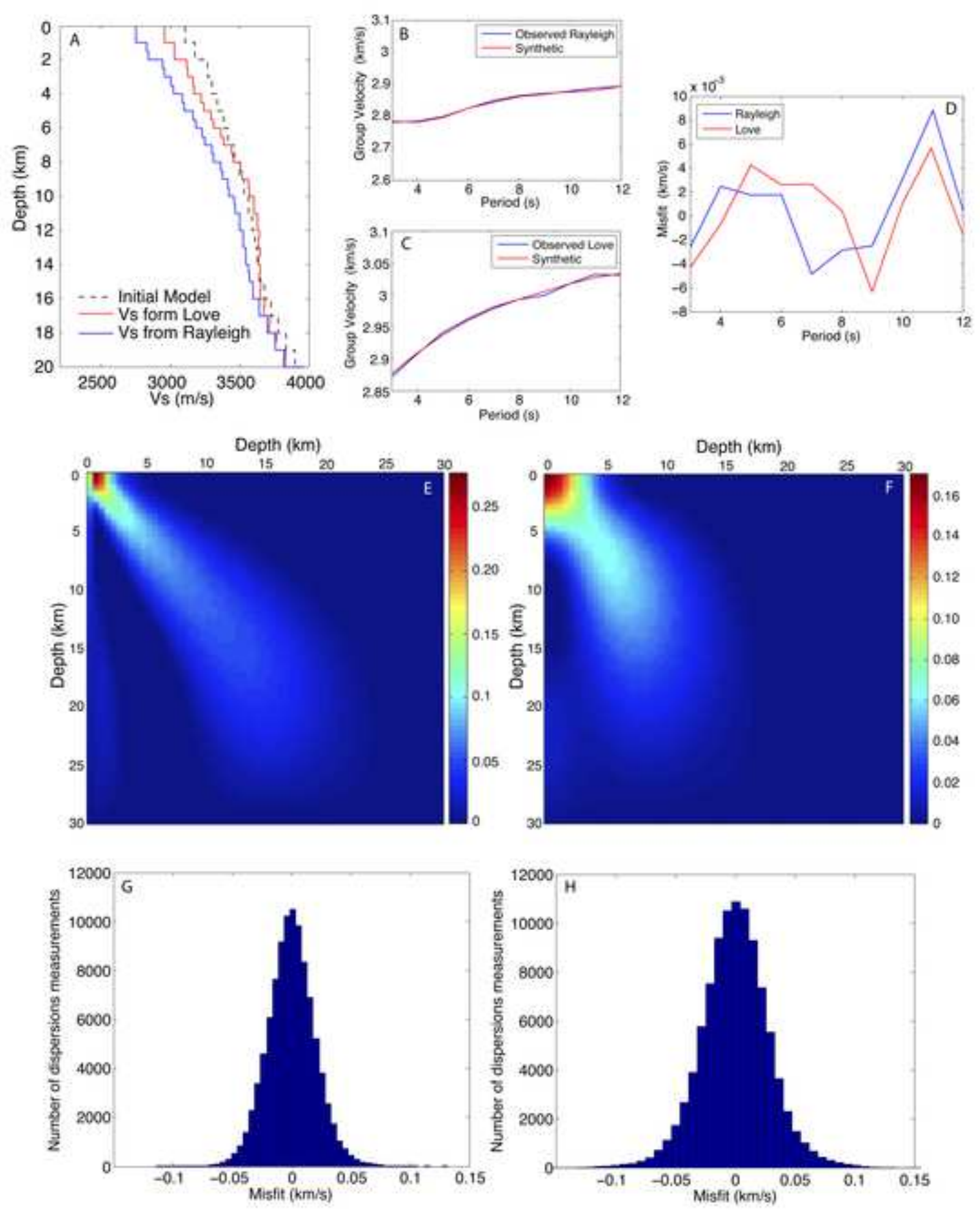


Figure 11
[Click here to download high resolution image](#)

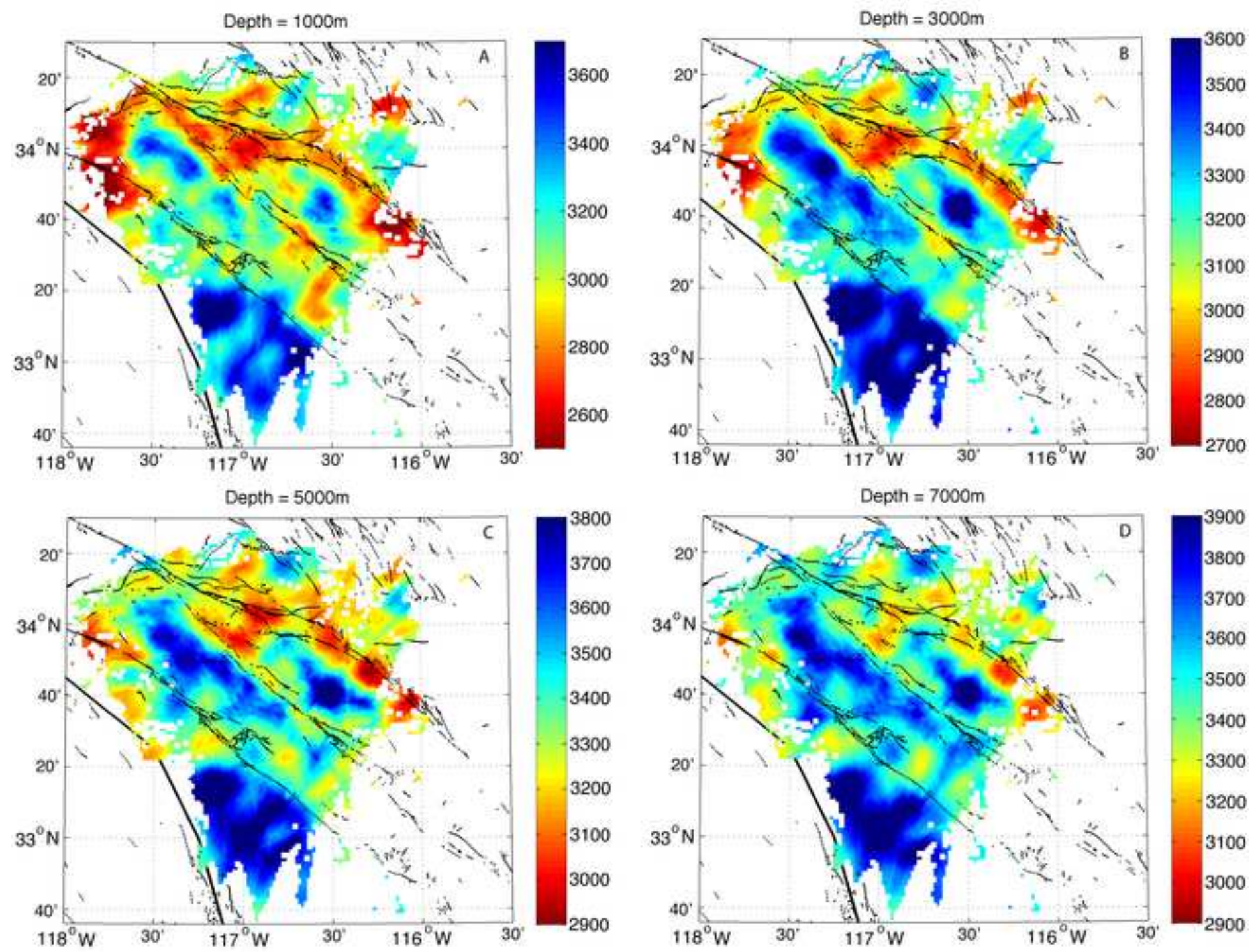


Figure 12
[Click here to download high resolution image](#)

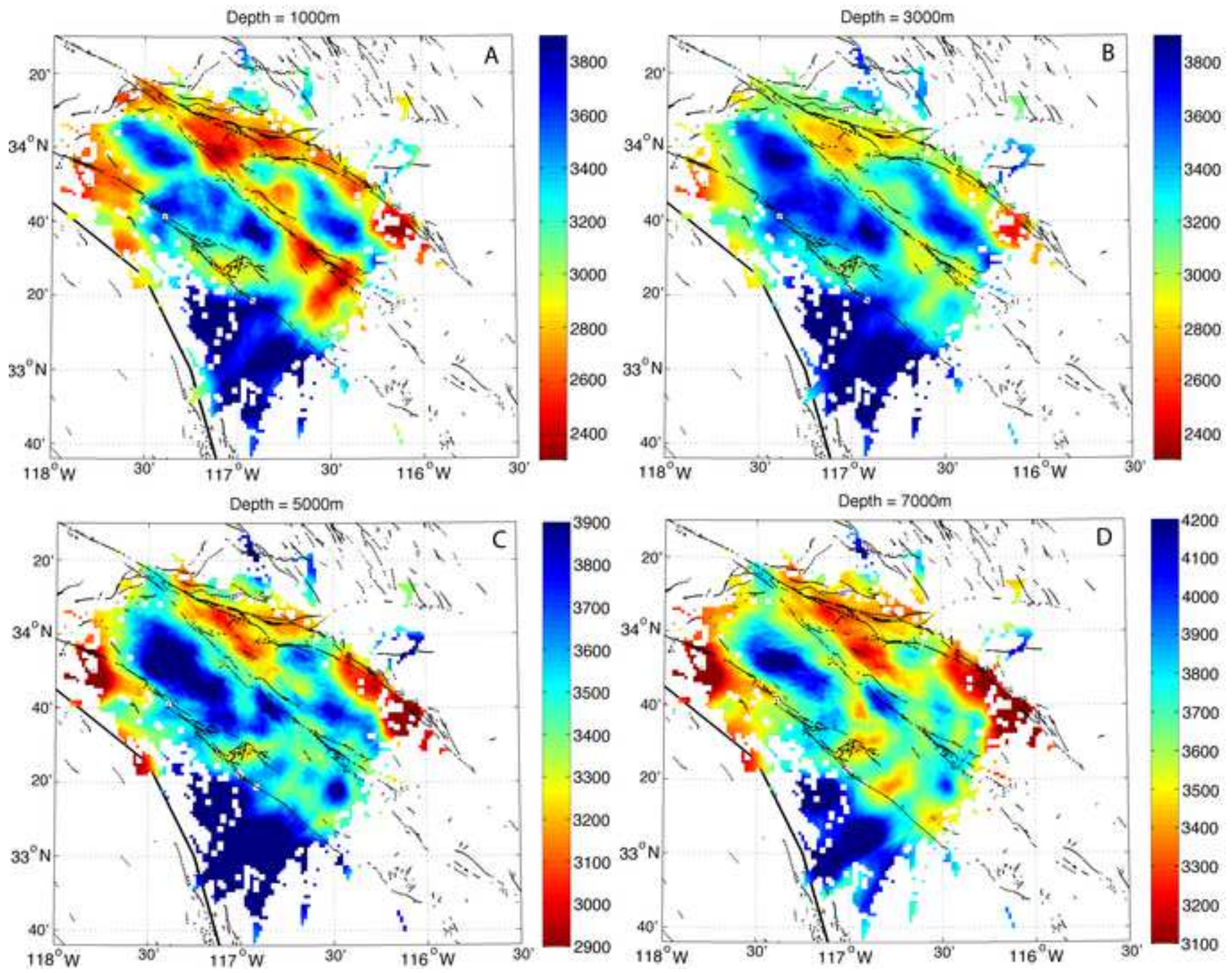


Figure 13
[Click here to download high resolution image](#)

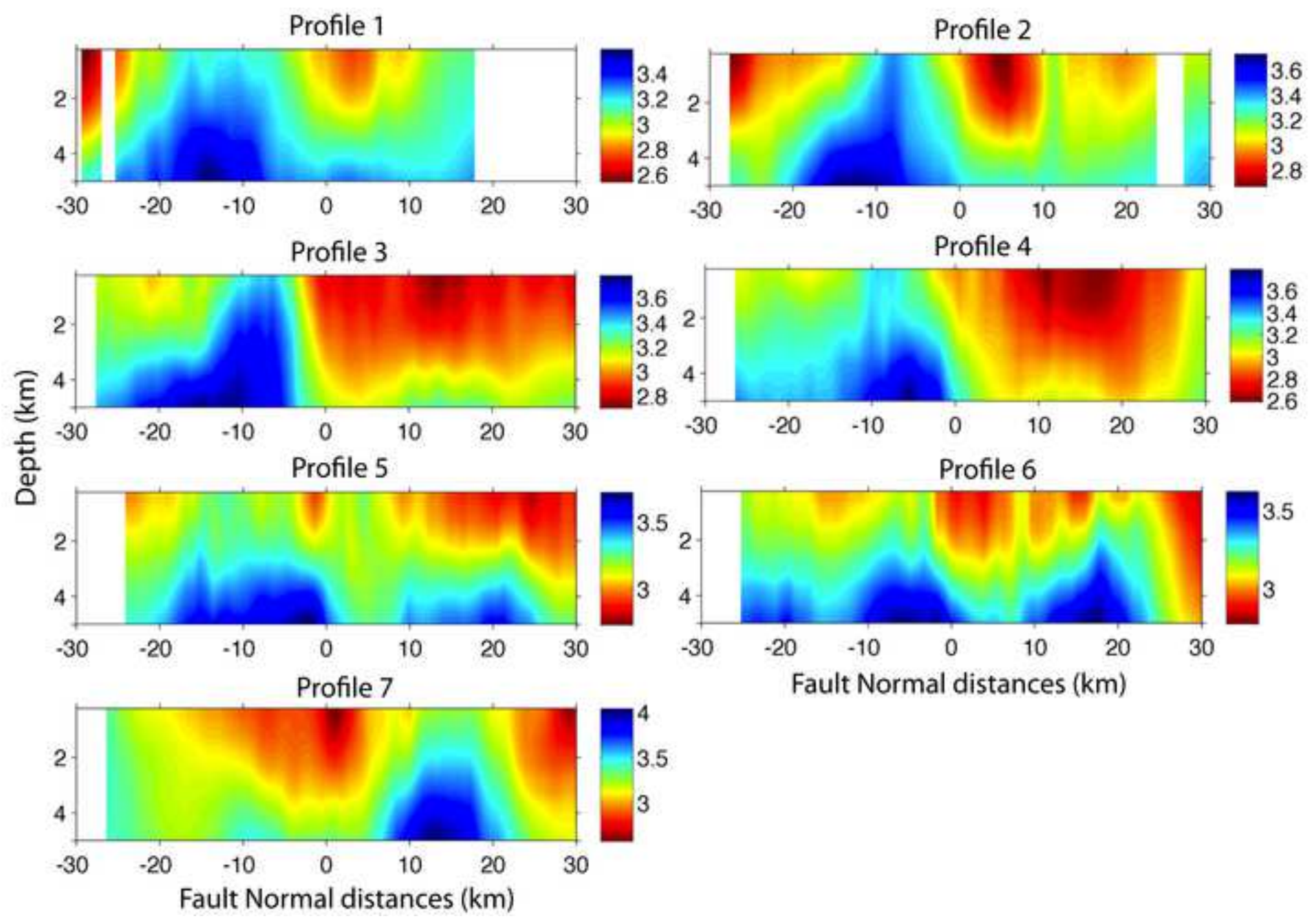


Figure 14
[Click here to download high resolution image](#)

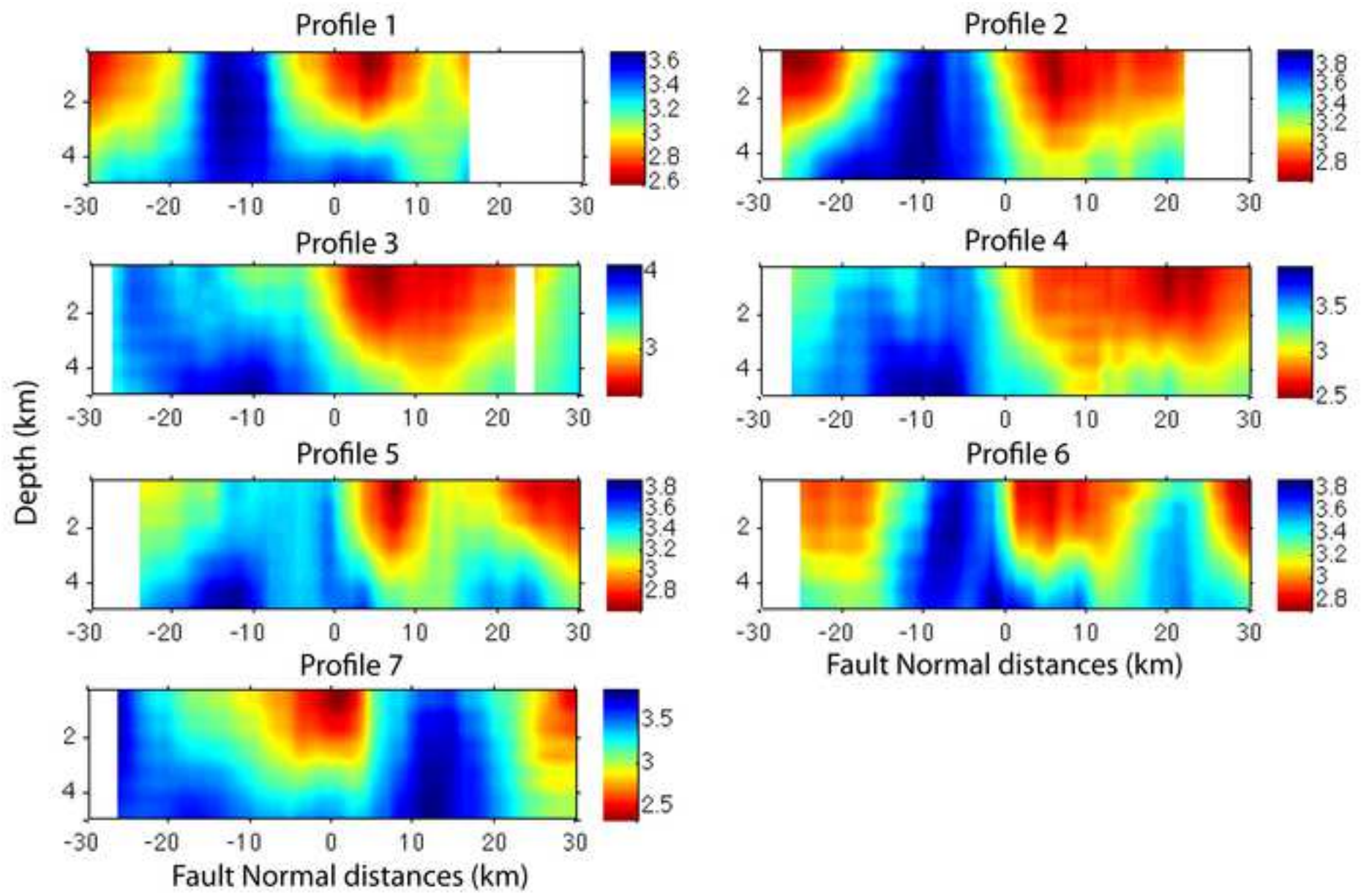


Figure 15
[Click here to download high resolution image](#)

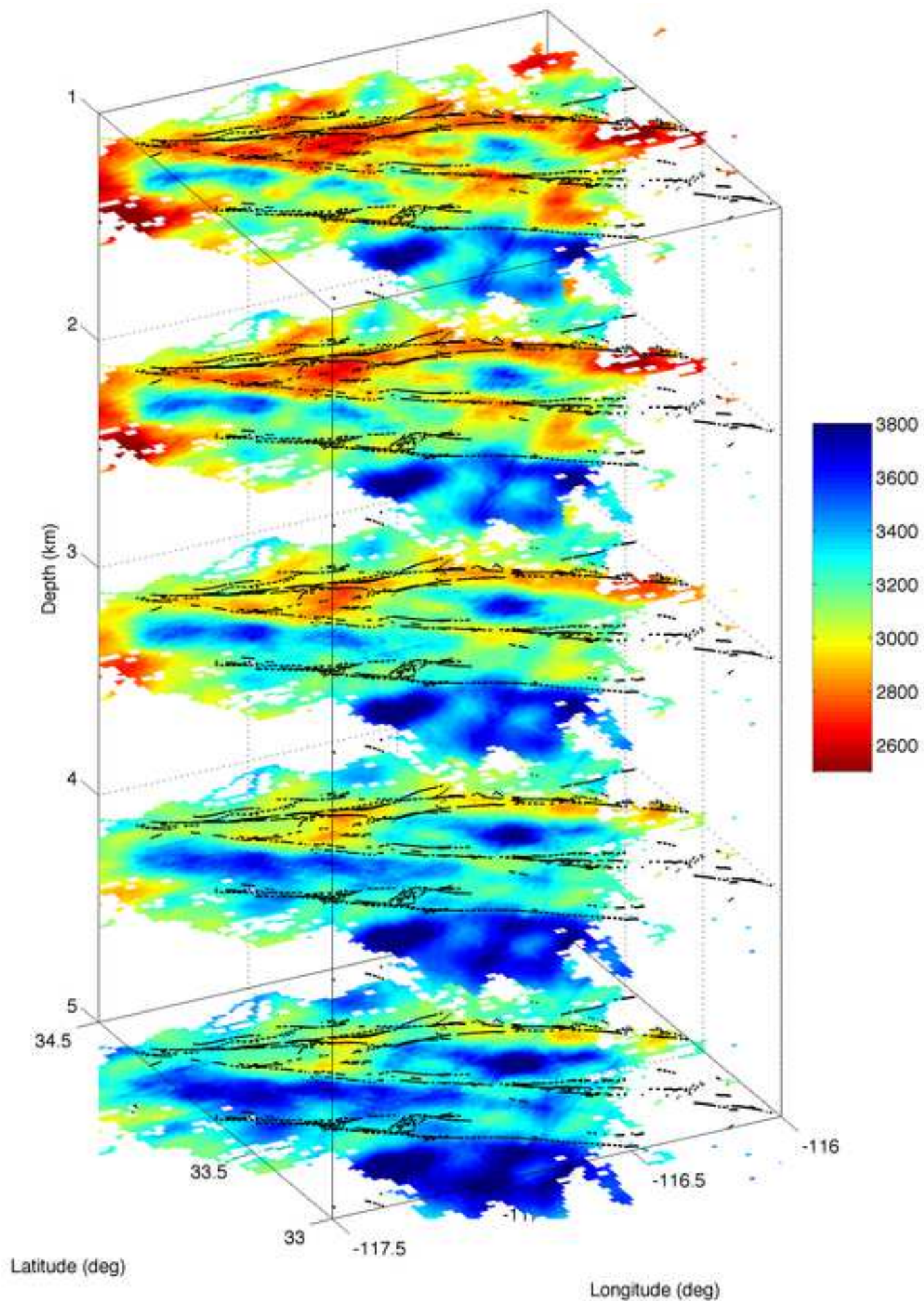


Table 1

[Click here to download Table: Table1.doc](#)

Period (s)	3	4	5	6	7	8	9	10	11	12
Love	2410	3068	3176	3122	3014	2858	2577	2322	1896	1457
Rayleigh	2881	4315	4542	4442	4182	3678	2781	2045	1379	810

Figure S1

[Click here to download Supplementary Material: figureS1.jpg](#)

Figure S2

[Click here to download Supplementary Material: figureS2.jpg](#)